

Chapter 1

The COMPASS Experiment

The CCommon Muon Proton Apparatus for Structure and Spectroscopy (COMPASS) experiment is a fixed target experiment located on the French side at CERN. COMPASS started taking data in 2002 in the same hall as earlier European Muon Collaboration (EMC), New Muon Collaboration (NMC) and Spin Muon Collaboration (SMC) experiments. COMPASS has studied hadron structure through (SI)DIS, Drell-Yan and Primakoff reactions and has done hadron spectroscopy measurements.

The COMPASS spectrometer is a two-stage spectrometer. The two stages are in a series and each stage contains various tracking detectors and as well at the end of each stage there is a muon wall filter for distinguishing between muons and other particles. Both stages also contain an electromagnetic and hadron calorimeter. Each stage is centered around a strong spectrometer magnet used for determining particle momentum. The first stage downstream of the target is the large angle spectrometer (LAS) and it is centered around the SM1 magnet which has an integrated field of 1 Tm. This stage detects tracks with larger polar scattering angles roughly between 26 mrad and 160 mrad. The second stage is the small angle spectrometer (SAS) and it detects particle tracks having a scattering angle between roughly 8 mrad and 45 mrad. This stage is centered around the SM2 magnetic which has an integrated field of 4.4 Tm. A graphic of the 2015 setup is shown in Fig 1.1.

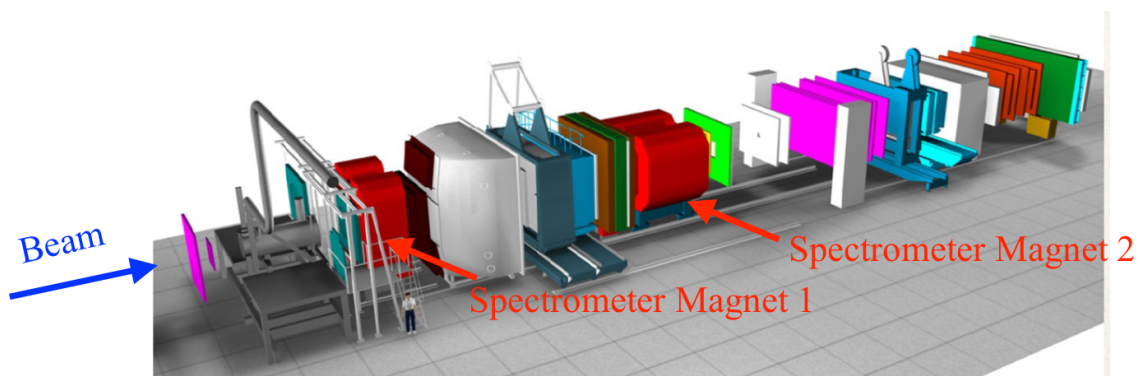


Figure 1.1: A schematic of the 2015 COMPASS setup

This chapter gives an overview of the COMPASS data taking setup with specific interest on the 2015 setup from which the data in this thesis was produced from. For a more thorough review of the spectrometer see reference [1]. This chapter is roughly organized by how the data taking occurs with an extra section on the unique features of the 2015 Drell-Yan setup in the end.

1.1 The Beam

The COMPASS spectrometer receives beam from the Super Proton Synchrotron (SPS) along on the M2 beam line. The Super Proton Synchrotron (SPS) is the second largest accelerator at CERN with a circumference of almost 7 km and it can accelerate protons up to an energy of 450 GeV. The SPS extracts beam to the Large Hadron Collier and as well sends beam to various experiments in the North Area at CERN. A schematic of the M2 beam line is shown in Fig. 1.2. There are several different beam types and energies available to COMPASS. The most common types used for physics analysis are a tertiary muon beam up to 190 GeV/c and secondary hadron beam with an energy up to 280 GeV/c . Both of these beam types can have a positive or negative charge. As well it is possible to have a lower intensity tertiary electron beam which is manly used for calibrations.

The start of the M2 beam line is the T6 target which is made of beryllium and has an adjustable length. The SPS accelerates primary protons up to 400 GeV/c which impinges on the T6 target to produce a secondary beam. The nominal proton intensity on the T6 target is $100 \times 10^{11} \text{ spill}^{-1}$. The longer the T6 target the higher the secondary intensity where 500mm is the longest and typical target length used for physics data taking. The reaction of the proton beam with the T6 mainly produces secondary protons, pions and kaons. Following this reaction a series of dipole and quadruple magnets are used to select the momentum and charge of interest.

The SPS spill structure varies throughout the data taking year depending mainly on the needs of the Large Hadron Colider (LHC). In 2015 the average intensity provided was $0.6 \times 10^8 \text{ s}^{-1}$ and the typical spill structure was two 4.8 second spills every 36 seconds.

1.1.1 Muon Beam

The muon beam is a tertiary beam which results from a weak decay of the secondary beam. After the initial proton reaction on T6 the resulting secondary particles are momentum and charge selected and sent through a 600m tunnel with focusing and de-focusing (FODO) quadruple magnets. In this tunnel the pion and kaons

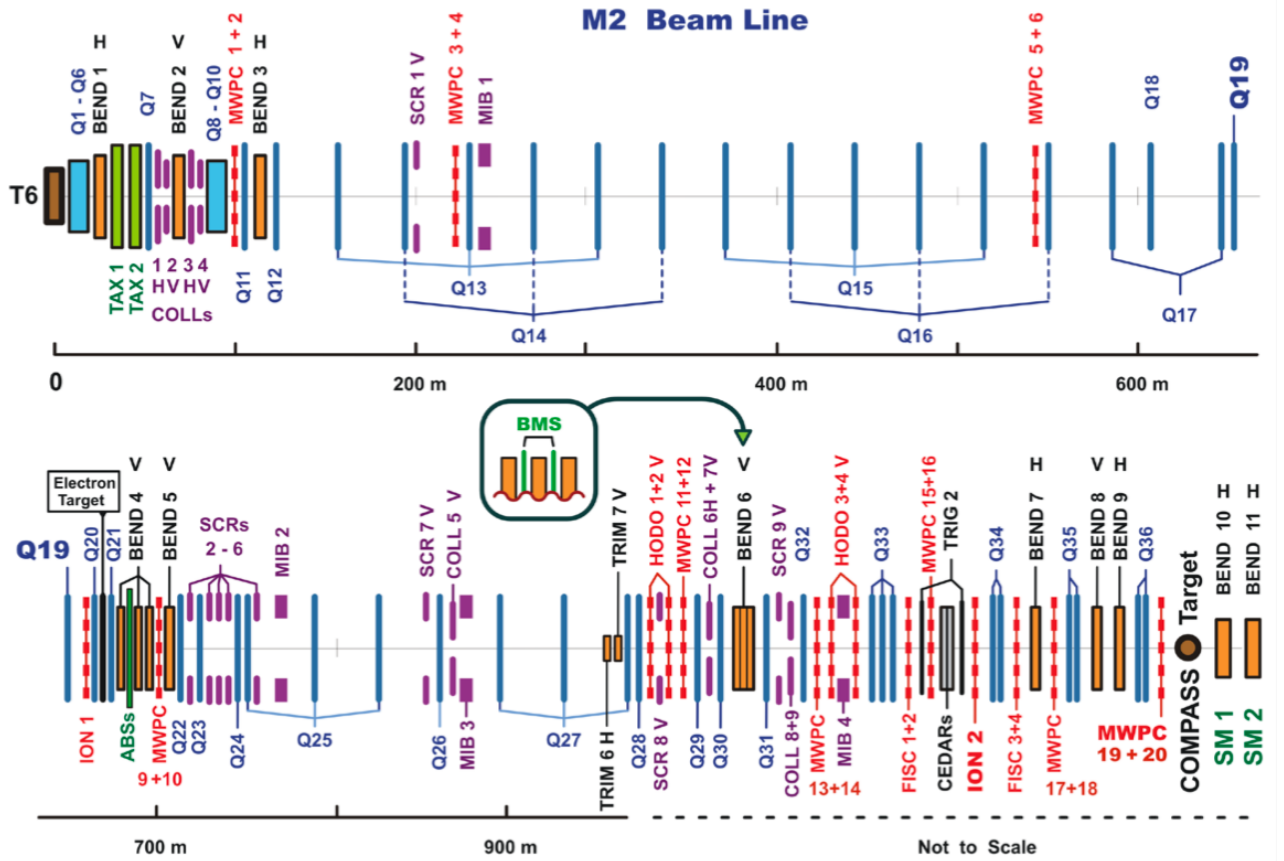


Figure 1.2: The M2 beam line at CERN

can decay as

$$\pi^{-(+)} \rightarrow \mu^{-(+)} + \bar{\nu}_{\mu^-}(\nu_{\mu^+}) \quad (1.1)$$

and

$$\kappa^{-(+)} \rightarrow \mu^{-(+)} + \bar{\nu}_{\mu^-}(\nu_{\mu^+}). \quad (1.2)$$

At the end of the tunnel a series of nine 1.1m long beryllium absorbers, referred to as the ABS in Fig. 1.2, remove the remaining hadron component of the beam which did not decay. A 172 GeV/c secondary beam

is chosen to achieve a $160 \text{ GeV}/c$ tertiary μ beam. Due to the fact that the neutrino in the reactions 1.1 and 1.2 is always left handed, the muon will be natural longitudinally polarized. For the muon momentum chosen the muon beam achieves a polarization of 80%.

1.1.2 Hadron Beam

In the case of a hadron beam the ABS absorbers are not used and the decayed muons are removed due to their lower momentum. In the case of a negative hadron beam the composition of the beam is approximately 97 % π^- , 2.5% kaons and 0.5% \bar{p} . The 2015 Drell-Yan data taking used a $190 \text{ GeV}/c$ hadron beam.

1.1.3 Additional Beam Line Components

After the decay tunnel the beam is bent upwards along another FODO tunnel of length 250m before reaching the surface approximately 100m before the COMPASS target. A series of three dipole magnets, called bend 6, then bend the beam to a horizontal position aimed at the COMPASS target. Both upstream and downstream of bend 6 are three tracking detectors (BM01-BM06) that make up the Beam Momentum Station (BMS). The BMS is the upstream most component of the COMPASS spectrometer and is able to determine the beam momentum to better than 1% of the beam momentum with an efficiency of approximately 93%. Bend 6 and the BMS are shown schematically in Fig. 1.3.

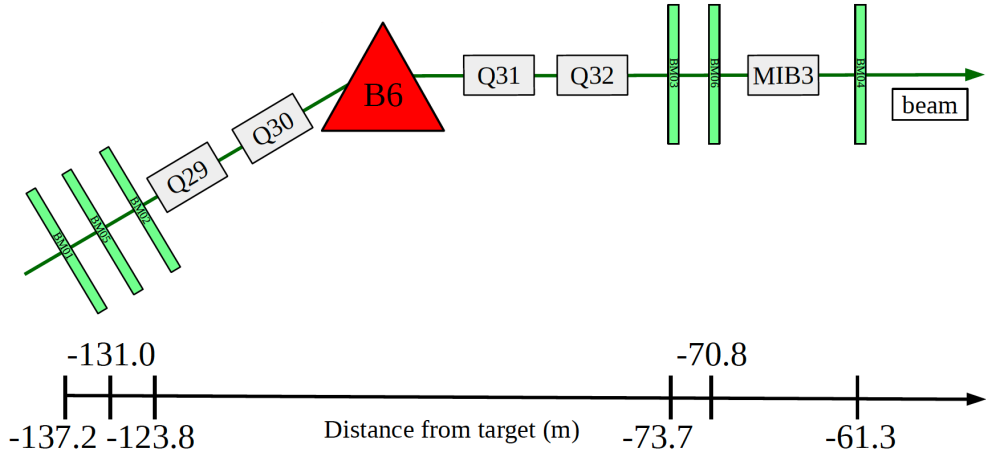


Figure 1.3: Bending the beam to a horizontal position. The BMS detectors are upstream and downstream of the bend 6 magnet.

For the 2015 Drell-Yan setup the π^- beam intensity was too high for the BMS station to work properly. For this reason special low intensity, approximately 10^6 s^{-1} , π^- beams were used in 2014 to determine the

momentum distribution for Drell-Yan data taking. The beam momentum distribution is shown in Fig. 1.4 where the average momentum is $190.9 \text{ GeV}/c$ with a spread of $\pm 3.2 \text{ GeV}/c$.

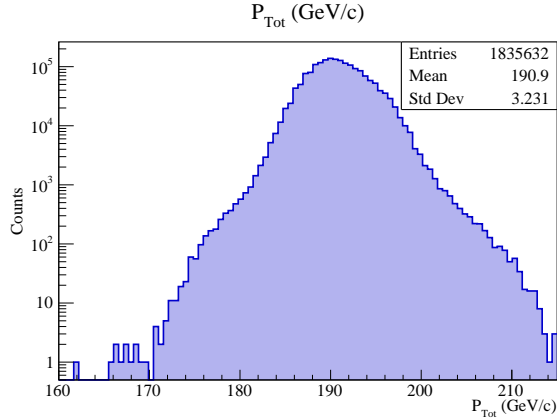


Figure 1.4: The momentum distribution of the π^- beam, determined during dedicated low intensity beam times.

Approximately 30 m upstream of the target are two Cherenkov counters (CEDAR) detectors. As the hadron beam has contamination from several components these CEDARs can be used to distinguish between these components. The CEDARs at COMPASS are high pressure detectors and have been demonstrated to achieve fast particle identification for particle momentums up to $300 \text{ GeV}/c$. The general principle of operation for the CEDARs is that two particles with the same momentum but different mass will emit Cherenkov radiation at different angles relative to their momentum. When a particle is traveling faster than the speed of light in a given medium it emits Cherenkov radiation in a cone centered along its momentum axis. The faster the particle is traveling the narrower the angle of the Cherenkov light cone. A schematic of the CEDAR operating principle is shown in Fig. 1.5. In 2015 the CEDARs were measured to be largely inefficient due to the high beam intensity.

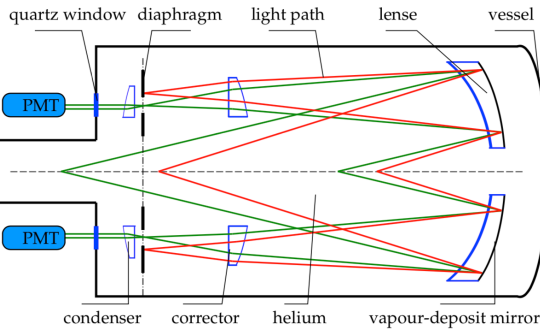


Figure 1.5: General principles of operation for the CEDARs at COMPASS. The red(green) lines correspond to Cherenkov light emitted from a particle.

For years with a transversely polarized target, such as 2015, a chicane system of dipole magnets is setup in front of the target. This is because a beam hitting the target without any angle would then be deflected inside the target to the left or right of the spectrometer. For this reason the chicane gives the beam an angle before hitting the target such that the non-interacting beam exits the target traveling straight towards the spectrometer.

1.2 The Polarized Target

The polarized target at COMPASS is the most complicated and essential component of the spectrometer. It is located upstream of the tracking detectors and spectrometer magnets and downstream of the beam telescope, described in section 1.3, detectors. The target consists of 2 or 3 cylindrical cells and the possible materials are either solid state ammonia (NH_3) or deuterated lithium (${}^6\text{LiD}$) or liquid hydrogen. Fig. 1.6 shows a schematic of the target.

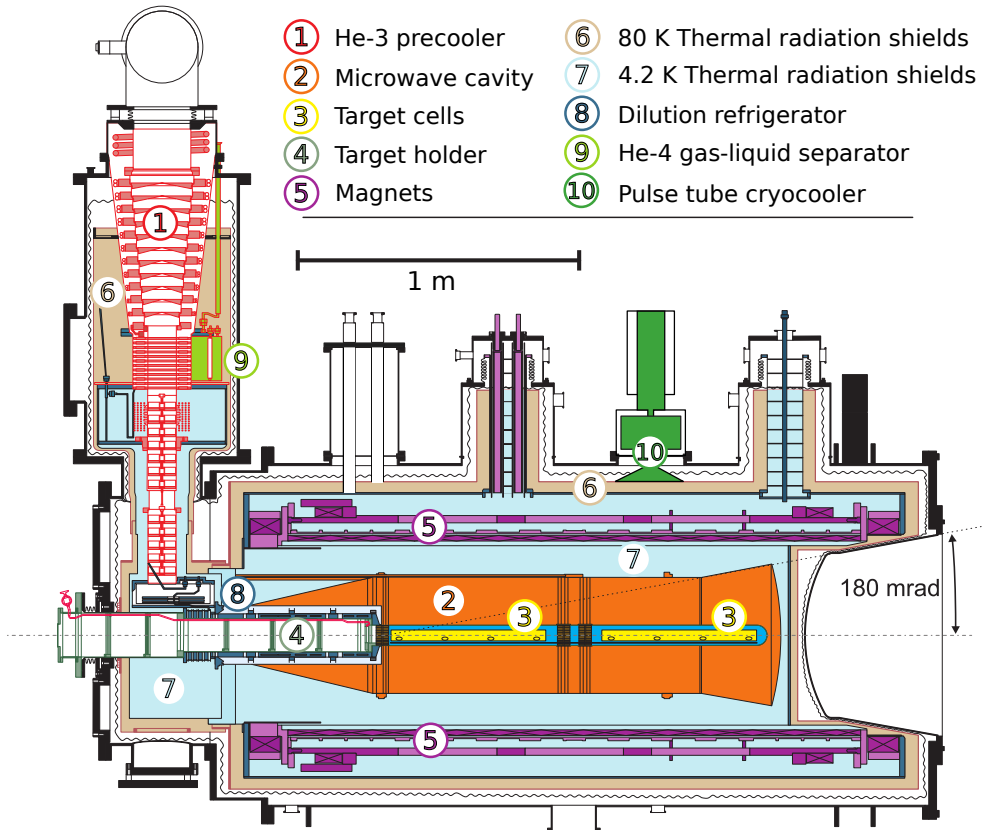


Figure 1.6: The polarized target at COMPASS

Surrounding the cylindrical cells is a longitudinal super conducting magnet capable of reaching a magnetic

field of 2.5T. This longitudinal magnet polarizes the target in the direction of the beam momentum and the target polarization is maintained by keeping the target in a liquid helium bath of approximately 60mK. This is called frozen spin mode where the temperature is maintained by a dilution refrigerator.

The target is polarized through the dynamic nuclear polarization (DNP) method [2]. This process works by first polarizing electrons in the target with the longitudinal magnet in the same longitudinal direction for all target cells while sending electromagnetic radiation in the microwave spectrum into the target. Due to their much lower mass, electrons have a larger magnetic moment and therefore can be polarized at a much faster rate than protons or neutrons. For atoms which have a nuclear spin it is then possible for these atoms to absorb a microwave going to an excited state with the electron spin anti-parallel to the magnet and the nuclear spin either parallel or anti-parallel to the magnet depending on the microwave frequency. The electron with the anti-aligned spin will then quickly have its spin realigned while the nucleon will take much longer to lose its polarization due to its smaller magnetic moment. This process can continue in this way resulting in a net nuclear polarization. Using the DNP method the target can achieve a polarization of approximately 90% in three days.

The target also includes a 0.63T transverse dipole magnet to change from longitudinal polarization to transversely polarized. The target must first be longitudinally polarized before the transverse target magnet can change the polarization direction. Once the target is transversely polarized, the target polarization can no longer be increased as microwaves can no longer shine on the target in the polarization direction. Therefore the polarization will decrease exponentially. In 2015 the target was polarized for about half a day between data taking sub-periods and achieved an average polarization of 0.73% which includes the effect of exponential polarization loss with time. The target transverse polarization relaxation time was about 1000 hours in 2015.

The target polarization was measured with 10 NMR coils while in longitudinal magnet mode. In the 2015, each target cell had the most upstream and downstream coils in the center of the target cell and the other three coils on the outside perimeter of the target cells as is shown in Fig. 1.7. Due to the fact that the polarization can only be measured with the longitudinal magnet on, the polarization is only measured at the start and finish of a transversely polarized data taking. The intermediate polarization are then determined by exponential interpolating between these two times.

In 2015 the setup was two transversely polarized target cells of 55 cm length and 2 cm in radius, separated by 20 cm and oppositely polarized. The polarization of the target cells was flipped every two weeks of data taking to reduce systematic effects. Due to the fact that the beam needs to be precisely steered onto the target anytime a beam line magnet is changed and that the chicane magnets upstream of the target are

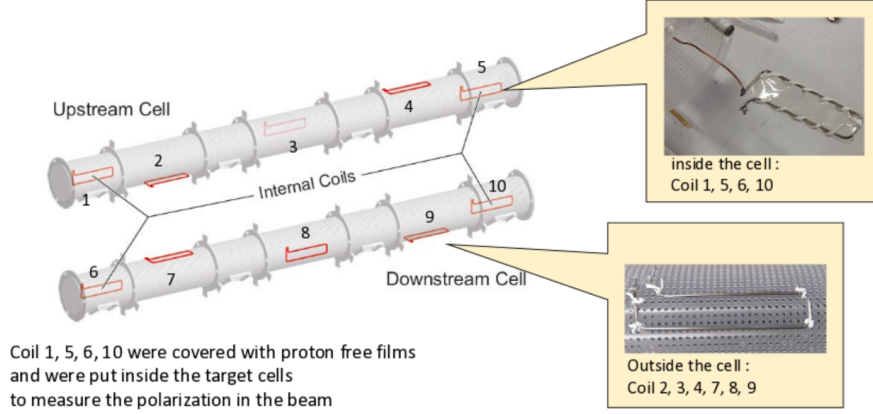


Figure 1.7: The empty polarized target cells side by side along with their NMR coil positions

setup for only one transverse target direction, the transverse target magnet only pointed downward in 2015. To achieve a polarization flip the target polarization had to therefore be rotated back to the longitudinal direction and the input microwaves had to be changed to achieve the desired polarization direction.

The target material in 2015 was NH_3 where the protons in the three hydrogen atoms were the only nucleons with nuclear spin. Therefore only some fraction of the target was able to be polarized and one would expect that this fraction is 3/17. However to get a more accurate determination of the dilution factor the follow calculation was used

$$f = \frac{n_H \sigma_{\pi^- H}^{DY}}{n_h \sigma_{\pi^- H}^{DY} + \sum_A n_A \sigma_{\pi^- A}^{DY}}, \quad (1.3)$$

where f is the dilution factor, n_H is the number of hydrogen atoms in NH_3 , n_A is the number of other nucleons in NH_3 , and $\sigma_{\pi^- H}^{DY}$ and $\sigma_{\pi^- A}^{DY}$ are the Drell-Yan cross-section for pion hydrogen scatter and pion nucleon scattering respectively. The cross-section were determined using a parton-level Monte-Carlo program MCFM [4]. The dilution factor was also further scaled down by studies of reconstruction migration between target cells. The average dilution factor in 2015 was 0.18.

1.3 Tracking Detectors

The goal of the tracking detectors is to determine a point in space where a particle traversed. The COMPASS tracking detectors attempt to do this for a wide range of angles, momentums and at different rates. For these reason there are several planar tracking technologies used at COMPASS which can be divided into three categories: very small angle tracker, small angle trackers and large area trackers. As the name suggest very small angle trackers measure tracks with small angle deflections from the beam axis which are essentially beam particles. The small area trackers measure particle tracks with low but non-zero angle have central dead zones. The large area trackers are several meters in height and width and measures the largest deflection angles up to 180 mrad.

All of these trackers are split into stations where each station corresponds to several detectors at roughly the same z-position along the beam line. Each station measures a track position in one or more orientation while most measure tracks in three or more orientations. The coordinate orientations measured are the X and Y coordinates which are the horizontal and vertical directions respectfully and as well the U and V coordinates which are rotated at different angles with respect the X and Y coordinates.

1.3.1 Very Small Angle Trackers

The very small angle trackers extend up to 3 cm away from the beam axis. This is the region with the highest number of tracking particles and therefore these detectors must be able to handle the highest rates up to 5×10^7 Hz. The two detector types that make up the very small angle trackers are either scintillating fiber detectors (SciFi) or silicon microstrip detectors. These two detector types are complementary to each other as the former have very good timing resolution while the latter have very good spacial resolution.

There are three silicon stations possible at COMPASS with active detecting areas of $5 \times 7 \text{ cm}^2$. The spacial resolution of these detectors is nominally $10 \mu\text{m}$ and the timing resolution is nominally 2.5 ns. For the 2015 setup, the beam intensity was too high for the silicon detectors to operate and therefore these detectors were not used in 2015.

There are 10 SciFi stations available at COMPASS with sizes varying from $3.9 \times 3.9 \text{ cm}^2$ to $12.3 \times 12.3 \text{ cm}^2$ planar areas. The fiber diameters vary between detectors and are 0.5 nm, 0.75 nm and 1 nm. Several fibers are bundled together to determine a strip hit position and the resulting nominal spacial resolutions are $130 \mu\text{m}$, $170 \mu\text{m}$ and $210 \mu\text{m}$. The nominal timing resolution of these detectors about 400 ps. In 2015 three SciFi stations made up the beam telescope and were placed upstream of the target to measure the beam trajectory and timing information. A fourth SciFi station was place in the LAS section of the spectrometer.

1.3.2 Small Angle Trackers

The small angle trackers are small area detectors that detect particles with a non-zero deflection angle. They cover 5 cm to 40 cm from the beam axis where the rate drops two orders of magnitude relative to the very small angle trackers to approximate 10⁵ Hz. At COMPASS there are two types of small area tracking detectors: micromesh gaseous structure (micromegas) and gas electron multipliers (GEMs).

There are three micromega stations at COMPASS all located sequentially after each other between the target and the first spectrometer magnet. All three detectors measure four coordinate projections and have an active area of 40x40 cm² with a 5 cm diameter dead zone. The micromegas operate by having a conversion region and a smaller amplification region. An ionized particle produced in the conversion region will drift through an electric field too small for amplification of around 3.2 kV/cm to the amplification region where the electric field is around 50 kV/cm and is high enough to amplify the signal which is then read out on strips. The conversion and amplification regions are separated by a metallic micromesh material. The electrons pass through the micromesh without resistance and are not rimmed out. The micromegas have good spatial resolution because the thickness of the amplification region is only 100 μm which is small enough to prevent the electron avalanche from spreading out much transversely between strips. The separation of the larger conversion region from the smaller amplification region with the micromesh prevents electric field lines from being distorted in the conversion region and therefore prevents the primary electrons from drifting slower in the conversion region. This allows micromegas to operate at a higher rate than would be possible otherwise. This principle of operation is illustrated in Fig. 1.8. The strips in the central part of the detector are 360 μm corresponding to a resolution of about 100 μm and the strips in the outer region are 460 μm corresponding to a resolution of about 120 μm . The nominal timing resolution 9 ns. In 2015 the micromegas were upgraded to include a pixelized section covering much of the dead zone area.

There are eleven GEM detectors located throughout the COMPASS spectrometer starting after the first spectrometer magnet down to the end of the spectrometer. These detectors are close to the beam axis and are mounted on a large area tracker covering the dead zone region of the large area tracker. All eleven detectors have an active area of 31x31 cm² and a 5 cm diameter dead zone. In times of lower beam intensity the dead zones can be turned on as an active area. The detector is split into four regions separated by a polyimide foil (50 μm thick) clad with copper on both sides with around 10⁴ cm⁻¹ drifting holes of 70 μm diameter. There is an electric potential of a few hundred volts between each foil layer. The GEM detectors speed up the amplification process by splitting the amplification avalanche into three locations thereby allowing for a higher rate of operation than would otherwise be possible. The electron amplification occurs around the holes of each of the three foil dividers which therefore speeds up the overall drift time from the

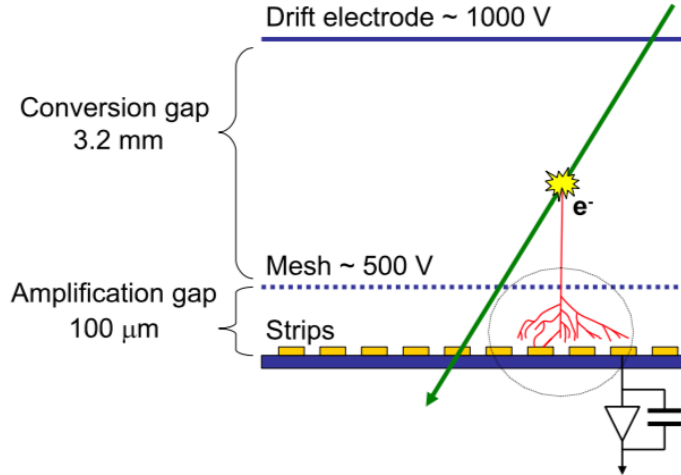


Figure 1.8: Principle of operation for the micromesh gaseous structures (micromegas)

ionization location to the strip readout. This principle of operation is shown in Fig. 1.9. The nominal timing and spacial resolution of the GEM detectors is 10 ns and 110 μm respectively. Two pixelized GEM detectors where also in operation but were not as crucial for the 2015 Drell-Yan measurement.

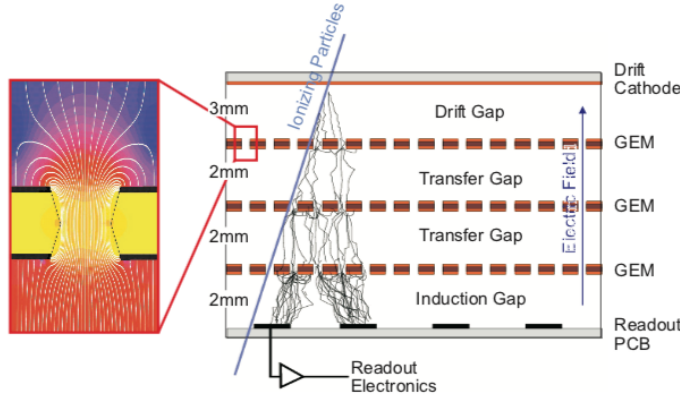


Figure 1.9: The operation principle of the gas electron multiplier (GEM) detectors

1.3.3 Large Area Trackers

The large area trackers measure the largest polar scattering angles at COMPASS. Their dead zones mostly coincide with a small area tracker, described in the previous section 1.3.2, which therefore means these detectors do not have to process the higher fluxes very close to the beam line. The most important feature

of these detectors is that they have a large planar area but as a consequence their position and timing resolution is not as good as the small and very small angle trackers. The types of large area trackers used are COMPASS are all gaseous detectors and include drift chambers (DCs), straw tube detectors (straws) and multi-wire proportional chambers (MWPCs).

The first four drift chambers downstream of the target are named DC00, DC01, DC04 and DC05. The first two, DC00 and DC01, have smaller active areas of $180 \times 127 \text{ cm}^2$ and a circular dead zone of 30 cm diameter and are positioned upstream of the SM1 magnet. The rates upstream of SM1 are higher due to low energy particles produced in the target, which are bent out of the acceptance of spectrometer by SM1. Therefore DC00 and DC01 need to be able to process a higher particle flux. The next two drift chambers, DC04 and DC05, are downstream of SM1 and both have larger active areas of $240 \times 204 \text{ cm}^2$ and as well have dead zones of 30 cm diameter. The active areas of all four of these DCs were roughly chosen to coincide with the acceptance of the SM1 yoke. DC05 was first installed for the 2015 Drell-Yan data taking and is further described in chapter ???. All four of these DCs measure four projection views corresponding to eight detector layers. A sketch of the principle of operation is shown in Fig. 1.10. The nominal spacial resolution for these detectors is $250 \mu\text{m}$.

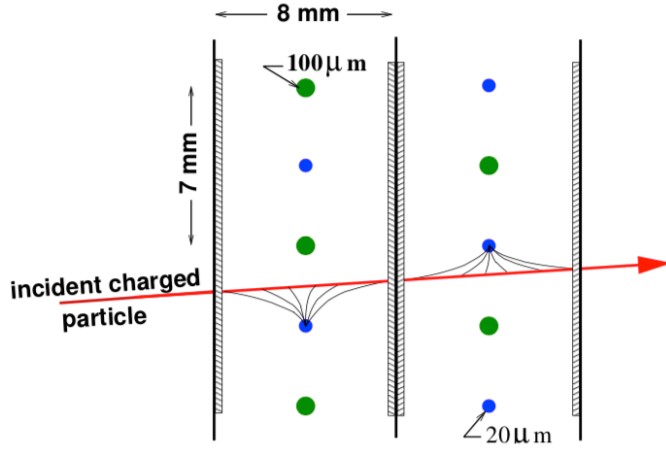


Figure 1.10: Drift cell of a Drift chamber with the ionized drift electron lines coming from the incident charged particle

There are additional drift chambers downstream of the SM2 magnet, named W45. W45 consist of six detector stations which each have an active area of $520 \times 260 \text{ cm}^2$ and a circular dead zone of 50 cm or 100 cm diameter. Each W45 station measure two projection views corresponding to four detector layers. The drift cells in W45 are $40 \times 10 \text{ mm}^2$ and the spacial resolution is nominally $1500 \mu\text{m}$.

In 2015 there were two straw stations in operation named ST03 and ST05. ST03 was in the large angle spectrometer after DC05 and consisted of two stations measuring six projection views. ST05 was in the small angle spectrometer and measured three projection views. The active areas of horizontal wire stations is $350 \times 243 \text{ cm}^2$ and the active area of the rotated wires is $323 \times 272 \text{ cm}^2$. The principle of operation for the straw detectors is very similar to that of a drift chamber however instead of having the detector made up of connected drift cells the straw detectors are made of circular tubes. Each tube consist of a gold plated tungsten anode wire in the center and the walls of the tube make up a cathode. Due to the fact that the cathode completely surrounds the anode wire there is no electrical interference between neighboring anode wires as there is for drift chambers. For this reason the electric field in each tube is easier to control and the ionized electron drift speed is more linear than other detectors. Each straw detector plane is divided into sections where the straw tubes in the outer most section from the beam line have a diameter of 9.6 mm and the tubes close to the beam line have a diameter of 6.1 mm. In additional in the central part of the detector there is a physical hole dead zone of $20 \times 20 \text{ cm}^2$. The nominal position resolution for these detectors is $400 \mu\text{m}$ and a frontal schematic is shown in Fig. 1.11. For the reason that most of the final state muon are reconstructed in the large angle spectrometer and the fact that many of the high voltage modules were not operation for ST05 in 2015, ST05 was not used for track reconstruction for Drell-Yan data.

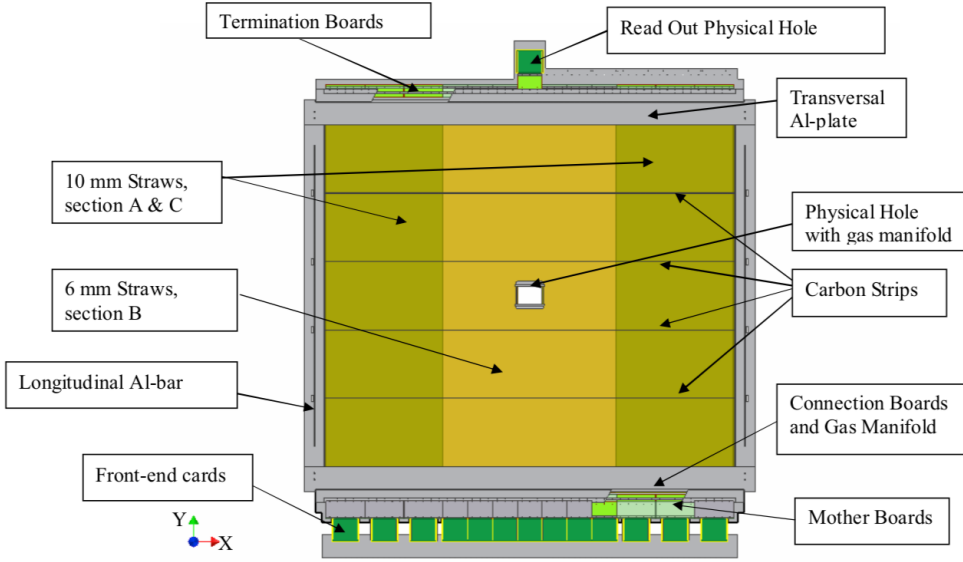


Figure 1.11: Front on view of a the active area of a straw detector at COMPASS

Another large area tracker that operates similarly to the straw tube detectors is the richwall detector. This detector is located before the SM2 magnet and after ST03 with an active area of $5.27 \times 3.91 \text{ cm}^2$ and a central dead zone of $1.02 \times 0.51 \text{ cm}^2$. The detector consist of eight layers of mini drift tubes (MDT) shown in

Fig. 1.12. The central part of each MDT includes a gold plated tungsten sense wire. The nominal position resolution of this detector is $600 \mu\text{m}$.

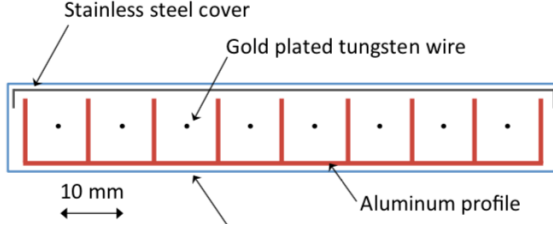


Figure 1.12: The richwall mini drift tubes

The final type of large area tracking detector at COMPASS is the MWPC. There are 14 of these stations located throughout the experiment. These MWPCs are separated into three categories distinguished by the coordinates they measure. The first type is called type A and consists of three projection views measuring an x, u and v coordinate. The second type is type A* and is the same as type A but measures the y coordinate in addition to the other three coordinates. Both type A and A* have active areas of $178 \times 120 \text{ cm}^2$. The final type is type B which has a smaller active area of $178 \times 90 \text{ cm}^2$ and measures the same projections as type A. There are seven stations of type A, one station of type A* and six stations of type B. All three types have circular dead zones of diameters 16 cm, 20 cm and 22 cm for types A, A* and B respectively.

The MWPCs operate on similar principles to the drift chambers but without a calibration drift curve. For this reason the MWPCs can be made to have one common gas volume between each station and their position resolution is determined as

$$\frac{\text{sense wire separation}}{\sqrt{12}}. \quad (1.4)$$

The separation between sense wires is approximately 2 mm which corresponds to a spacial resolution of these detectors around $600 \mu\text{m}$.

1.4 Particle Identification

In the COMPASS spectrometer there are four types of detectors used to determine particle identification (PID): the ring image Cherenkov (RICH) detector, electromagnet calorimeters (ECAL), hadron calorimeters (HCAL) and muon walls (MW). The RICH distinguishes between pions, kaons and protons; ECAL1 and ECAL2 measure the energy from photons and electrons; HCAL1 and HCAL2 measure the energy from

hadrons; and MW1 and MW2 distinguish muons from all other particles. The RICH, ECAL1, HCAL1 and MW1 are in the large angle spectrometer in that respective order along the beam line. The small angle spectrometer includes ECAL2, HCAL2 and MW2 again in that respective order along the beam line.

The RICH detector operates similarly to the CEDARS, section 1.1.3, in that Cherenkov radiation is emitted from particles traveling through the RICH at an angle dependent on their velocity. The RICH is filled with a dielectric gas, C_4F_{10} which has an index of refraction greater than air. The momentum of particle going through the RICH is determined from bending angle around SM1 and therefore the mass of particles can be distinguished once the RICH determines the entering particles velocity. A sketch of the RICH and its operating principle is shown in Fig. 1.13. To distinguish between particles the minimum momenta are: 2.5 GeV/c for pions, 9 GeV/c for kaons and 17 GeV/c for protons. The maximum momentum the RICH can distinguish between any of these particles is 50 GeV/c. This detector is located in the large angle spectrometer before any calorimeters.

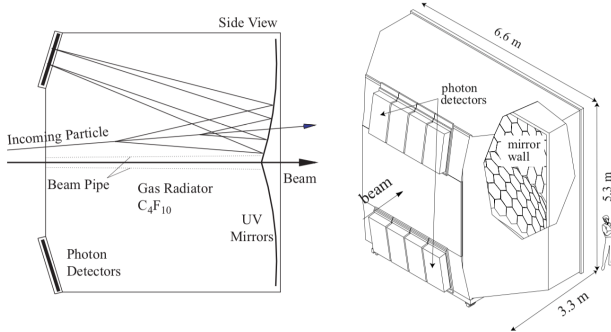


Figure 1.13: Side view demonstrating the principle of operation of the RICH detector.

The ECALs and HCALs both stop specific particles of interest where the energy deposited in each respective calorimeter is proportional to the incoming particle's energy. This energy knowledge along the momentum determined from the tracking detectors allows to determine particle identification. The ECALs and HCALs can therefore measure the energy of incoming particles. The ECALs are made of lead glass towers with photon multipliers attached to these towers on one side. An incoming photon or electron interacts with the lead glass to produce a light signal which is readout with these photon multipliers. Other particles also interact with the material in the ECALs however hadrons and muons are able to exit through the detector

unlike photons and electrons. A frontal view of ECAL1 is shown in Fig. 1.14 and a frontal view of ECAL2 is shown in figure Fig. 1.15.

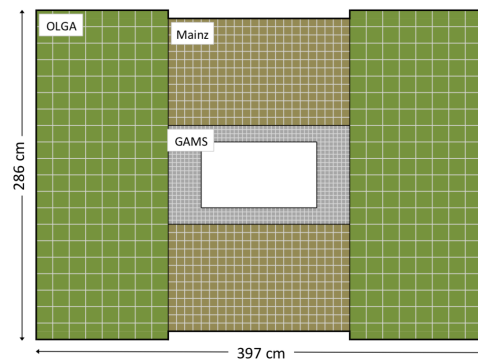


Figure 1.14: Frontal view of the electromagnetic calorimeter 1

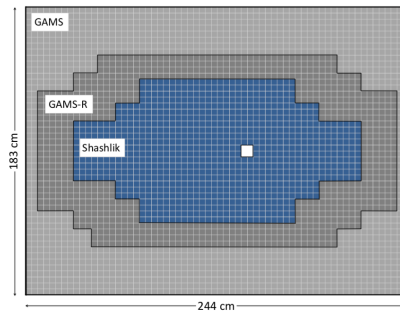


Figure 1.15: Frontal view of the electromagnetic calorimeter 2

The HCALs are sampling calorimeters which are made of alternating layers of iron and scintillating material. An incoming hadron deposits all its energy in the HCAL by making a particle showers in the iron which are detected by photo multipliers connected to the scintillating material. The HCALs are placed after the ECALs in each stage of the spectrometer because an electromagnetic shower happens faster than a

hadronic shower. The HCALs are affect at determining particles energy from particle with energies between 10 GeV and 100 GeV.

The two MWs are located after an HCAL in their respective stages. Due to their higher mass and absence of color charge, muons are able to pass through the most material budget of any of the particles detected at COMPASS. For this reason both MWs consist of an absorber and tracking detectors downstream of this absorber. Any particles that make it through the absorber are with a very high probability muons. MW1 consists of eight tracking planes before a 60 cm iron absorber and same number of tracking planes after this absorber. The tracking portions of MW1 are build similarly to the richwall, described in section 1.3.2, in that they are also made of MDT modules. The active area of MW1 is $480 \times 410 \text{ cm}^2$ and includes a dead zone of $140 \times 80 \text{ cm}^2$. Each plan of this detector has a spacial resolution of 3 mm. A sketch of MW1 is shown in Fig. 1.16. The second muon wall, MW2, is located downstream of a concrete absorber which 2.4 m thick. MW2 consists of 12 planes with and active area of $450 \times 450 \text{ cm}^2$ and a dead zone of $90 \times 70 \text{ cm}^2$. The detector operates similarly to the straw detectors, section 1.3.2, in that it is made of drift tubes with a wire in the center of these tubes. The diameter these drift tubes is 29 mm and the position resolution is about 1.4 mm.

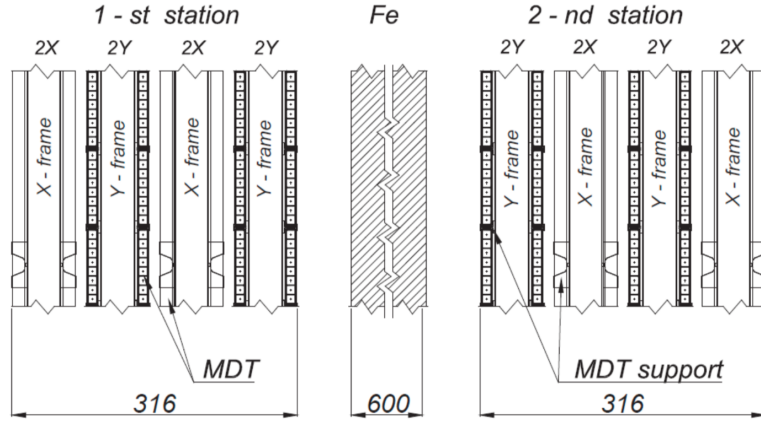


Figure 1.16: A side view sketch of the muon wall 1 detector

There is one last absorber in the COMPASS spectrometer located before the H5 hodoscope at the end of the spectrometer hall. This absorber is called muon filter 3 (MW3) and ensures that the inner trigger is only triggered by a muon.

1.5 Trigger

The trigger system at COMPASS defines what is an event. Whenever the trigger signal is given, all the detector information within a few nanosecond timing window is recorded. Due to the fact that there are very many background events occurring as the beam impinges on the target, there is too much information going to the front end modules (FEMs) of the detectors for the FEMs to process and record all the information. For this reason only a certain subset of all the information is stored to disk. The trigger system must therefore have good timing resolution to make quick decisions on which data to record. At COMPASS a system of scintillating hodoscopes attached to PMTs is used as the trigger. The timing resolution of these detectors is approximately 1 ns. A top view schematic of COMPASS showing where the relative position hodoscopes for each trigger is shown in Fig. 1.17.

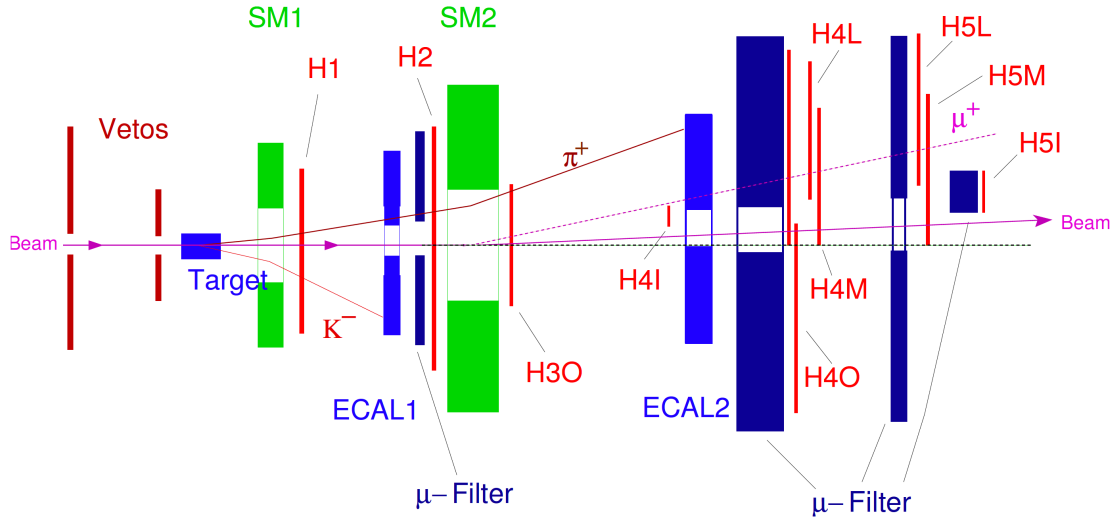


Figure 1.17: Top view of the spectrometer highlighting how different particles can signal a trigger

At COMPASS there are five different triggers used to register physics events. Each trigger type includes at least two hodoscopes at different z-positions in the spectrometer. The types of triggers are either target pointing, when the hodoscope slabs are horizontal; or energy loss, when the hodoscope slabs are vertical. The target pointing trigger is setup used with higher polar scattering angles to signal an event if a particle is scattered from the target and the energy loss trigger is setup used with lower Q^2 interactions to signal an event if a particle is bent a specified amount. This concept is illustrated in Fig. 1.18. There are four triggers in SAS: the inner trigger (IT), the middle trigger (MT), the ladder trigger (LT) and the outer trigger (OT). The IT is an energy loss trigger and includes the hodoscopes HI04X and HI05X. The MT includes both energy loss and target pointing slabs. The hodoscopes in the MT are HM04X, HM05X, HM04Y and HM05Y. The LT includes target pointing slabs and the hodoscopes are HM04Z, HM05Z, HM04A and HM05A. The OT is an energy loss trigger and includes the hodoscopes HI04Z and HI05Z.

HM05Y. The MT hodoscopes whose names end with an X have vertical slabs and those ending with a Y have horizontal slabs. The LT is an energy loss trigger which consists of HL04X and HL05X. The final trigger in SAS, the OT, is a target pointing trigger and consists of hodoscopes HO03Y and HO04Y. The remaining trigger system is in LAS and is a target pointing trigger consisting of hodoscopes HG01Y and HG02Y. The kinematic coverage for the 2015 triggers is shown in Fig. 1.19.

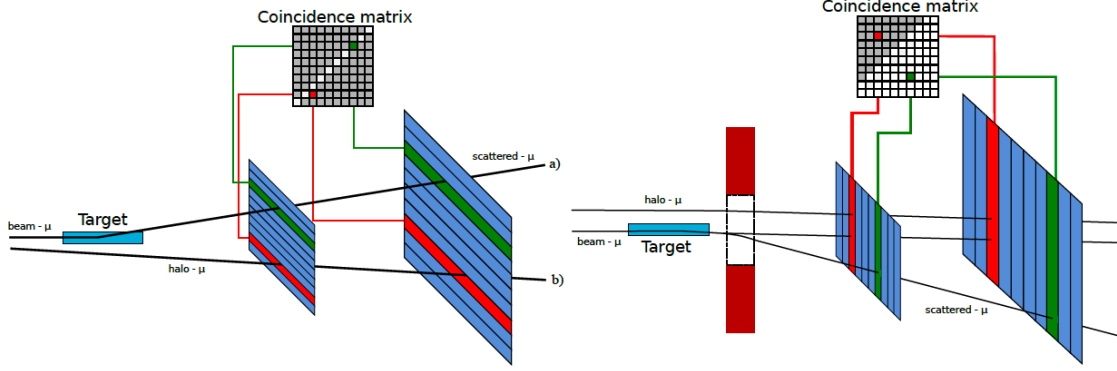


Figure 1.18: The two types of triggers (left is target pointing and right is energy loss) at COMPASS and an illustration of the coincidence matrix used to select events of interest

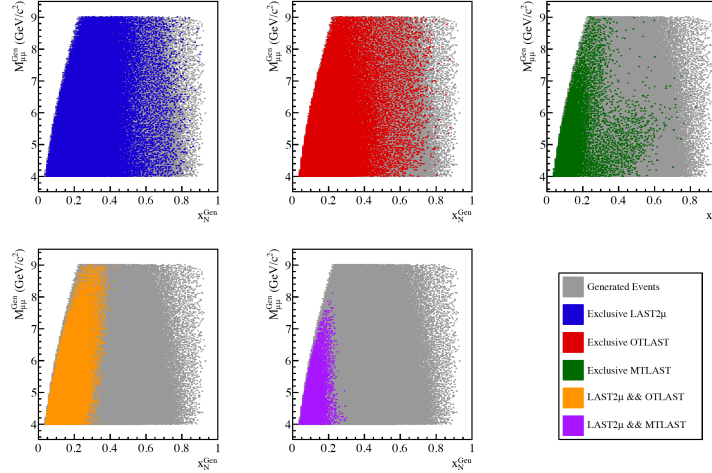


Figure 1.19: The kinematic coverage for the 2015 triggers determined from Monte-Carlo studies

There is also a veto system upstream of the target as shown in Fig. 1.17. This veto trigger consist of hodoscopes attached to PMTs as well. It is centered on the beam axis but with not active area in the nominal beam line. The veto trigger is used to reject halo muons. Halo muons occur from the beam decaying, as in Eq. 1.1 and Eq. 1.2, where this decay occurs upstream of the target but downstream of the ABS absorbers. The muon halo surrounds the hadron beam due to its lower momentum which allows the veto hodoscopes outside of the beam line to reject these type of events.

In addition to the five trigger systems based on hodoscopes is the calorimeter trigger (CT). The CT can be used as a trigger when a particle deposits more than a certain energy threshold in one of the calorimeters. In 2015 this trigger was only used as an independent study of the other triggers at COMPASS.

In 2015 setup the Drell-Yan process of interest corresponds to two detected muons. For this reason two triggers must signal a particle in coincidence for an event to be registered. For physics analysis the coincidence triggers are either two muons in LAS (LASxLAS), one muon in LAS and one in the OT (LASxOT) or one muon in LAS and one muon in the MT (LASxMT). The LASxLAS trigger system covers the high Q^2 and high x_{beam} phase space and the triggers including a SAS hodoscope cover lower Q^2 values. In addition to these three dimuon triggers where three single muon triggers corresponding to a particle in LAS, MT or OT. These three triggers however were pre-scaled down to only take every 500, 100 or 100 events respectively. For further tests 2015 included a random trigger and a beam trigger which was scaled down by 35000.

1.6 Data Acquisition

The data acquisition (DAQ) collects data from the over 250,000 detector channels and transfers this data to storage on magnetic tape at CASTOR (CERN Advanced STORage). Despite the triggering system used to reduce the data rate, the data rate still ranges from 10 kHz to 100 kHz with a typical event size of 45 kB. The DAQ is designed to handle these rates and data size while minimizing the dead time associated with data collection and transfer. In 2015 the dead time was approximately 10% and the DAQ recorded approximately 750 terabytes of raw data after the spectrometer finished commissioning time.

Data collection begins with the digitization of information from a detector channel eight by a time to digital converter (TDC) or an analogue to digital converter (ADC). These TDCs and ADCs are eight on the detector FEMs or on custom COMPASS readout electronics named: GANDOLF (Generic Advanced Numerical Device for Analog and Logic Functions), GeSiCA (Gem and Silicon Control and Acquisition) or CATCH (COMPASS Accumulate Transfer and Control Hardware). After digitization the data is transferred by optical fibers to an FPGA multiplexer where the data is buffered by spill and arranged by event. From there an FPGA switch sends the data to multiplexer slaves. The slaves are online computers that oversee the final steps for raw data and transfer this data to CASTOR. This whole process is shown schematically in Fig. 1.20.

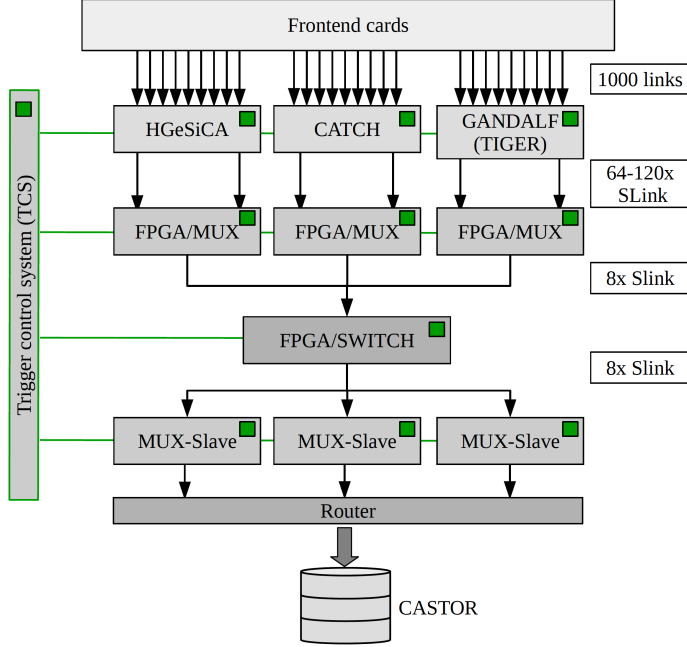


Figure 1.20: The data acquisition steps at COMPASS

1.7 Data Reconstruction

The COMPASS Reconstruction and AnaLysis Program (CORAL) reconstructs the raw data into physical quantities such as particles with momentum and charged and possibly an originating vertex location [3]. The raw data from the DAQ is digitized timing information from tracking detectors or digitized energy information for calorimeters. The process of reconstructing tracks takes the timing information and determines a position in space for a particular tracking detector based on a calibration. CORAL then uses a Kalman Filter to determine straight tracks in regions with no or low magnetic field [5]. The tracks are then connected through the magnetic field using a fast lookup table for known possible bending radii. At this point a track is determined to have a momentum, charge and a χ^2 value associated with the track. From there the tracks are extrapolated back to the target region and the intersect of two tracks is determined as a vertex. If in addition to the two intersecting tracks a beam particle can be extrapolated forward to the same vertex location then the vertex is assigned to be a primary vertex otherwise the vertex is defined as a secondary vertex. This reconstruction stage reduces the data volume by approximately a factor of 10. A diagram of the reconstruction data flow is shown in Fig. 1.21. In 2015 there were several data reconstructions performed. Between each reconstruction improvements were made to detector calibrations, detector alignment, beam tracking and any other preprocessing improvements that could be made. The final two productions are the t3 production and the slot1 production. The results shown in this thesis are from either t3 or slot1.

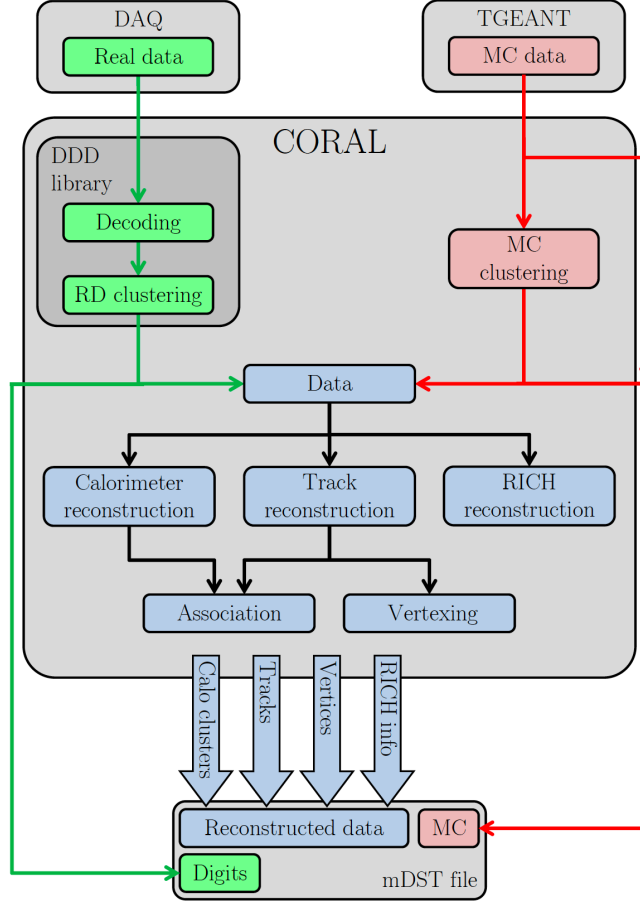


Figure 1.21: The schematic of the CORAL reconstruction process

Once reconstruction has been performed the data is stored in data structured trees (DSTs). The usual procedure of reconstruction which gives physical values momentum and charge to tracks results in data called miniDSTs. There is the possibility to save more information, for example detector hit location information, to make so called fatDSTs. These DSTs are now in a format which can be processed by PHAST (PHysics Analysis Software Tool) which is COMPASS program written to further analyze physics data. With PHAST there is the possibility to loop over all the miniDSTs and make certain cuts to produce so called μ DSTs. In 2015 μ DSTs were made for all the analysis data where a cut was applied to the miniDSTs saving only events with at least two muons. Both CORAL and PHAST are fully object-oriented C++ programs.

1.7.1 Monte-Carlo Production

Monte-Carlo data is simulated data which is performed in three steps. First a programs generates specific physics processes based on their theoretical probabilities. The generators of Monte-Carlo used for this thesis

are PYTHIA versions 6 and 8 [6]. Next a GEANT4 simulation of COMPASS determines if a detector will register a hit from these generated physics processes. This saves the data in a raw data format which can be reconstructed by CORAL. Finally the simulated data is reconstructed by CORAL and analyzed in PHAST the same as if the data were real data.

1.8 2015 Drell-Yan Data Taking

The 2015 Drell-Yan data taking is one of the main programs for the COMPASS-II experiment. The data taking began in April of 2015 and ended in November of that year. The physics data used for analysis started in July and finished at the end of data taking while the data before July was used for calibrations and commissioning. The total analysis data was split into nine data periods labeled W07-W15 where each data period corresponded to approximately two weeks of beam time. The spin orientation of each target cell was reversed after the first week of every period to reduce systematic effects arising from different geometric acceptances and luminosities of up and downstream target cells.

1.8.1 Hadron Absorber

The previous sections in this chapter described the spectrometer setup generally and mentioned the specifics for the 2015 setup. The main unique hardware addition in 2015 is the hadron absorber. The hadron absorber was installed because the beam intensity is high resulting in many strong interactions in the target and therefore the first tracking detectors upstream of SM1 have occupancies which are too high for tracking. Therefore the hadron absorber was installed to prevent all particles except muons from entering the spectrometer.

The hadron absorber was placed just downstream of the two target cells as can be seen in Fig. 1.22. The absorber corresponded to approximately 7.5 interaction lengths of material where the material was mostly alumina (Al_2O_3) and concrete. Inside the absorber was an aluminum target followed by a tungsten plug, each of radius 2.5 cm. The tungsten was used as a beam dump while the aluminum was present to prevent back scattering from the tungsten beam plug. A side view showing the dimensions and materials used can be seen in Fig. 1.23. Both the aluminum target and tungsten plug served the double purposes as absorbers and also as unpolarized nuclear targets. In addition to the hadron absorber two thin ${}^6\text{Li}$ absorbers were added just downstream of the primary absorber to absorb thermal neutrons produced in the primary absorber. This ${}^6\text{Li}$ absorber was proposed to improve the performance of the first tracking detector downstream of the target even with the hadron absorber installed.

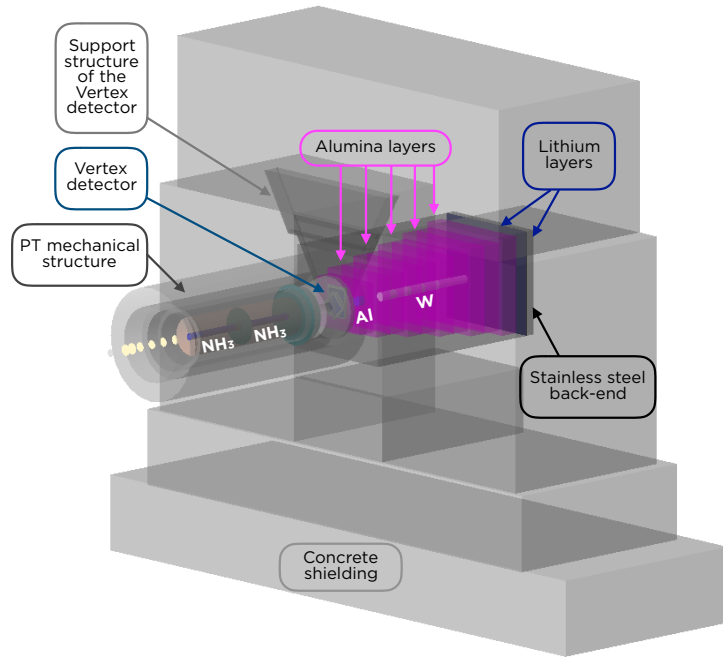


Figure 1.22: The hadron absorber downstream of the polarized target in 2015

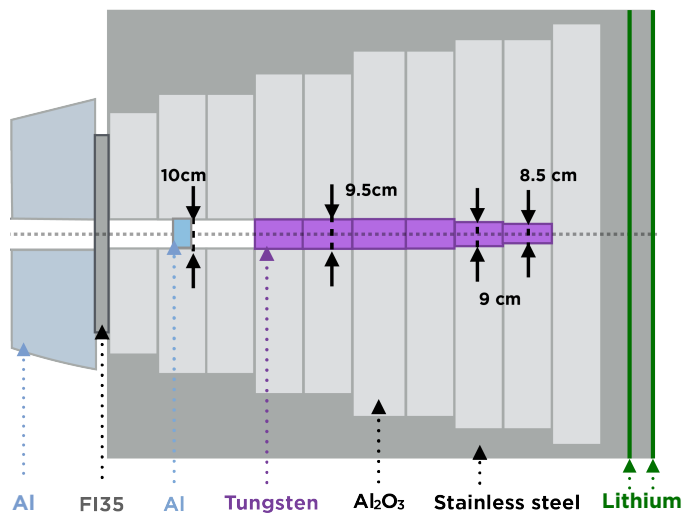


Figure 1.23: Side view of the hadron absorber used in 2015

Chapter 2

Measurement of the Left-Right Asymmetry in the Drell-Yan Process

Introduction about L/R asym. In this Chapter.... Define AN

2.1 Data Sample

The data sample is from the 2015 COMPASS Drell-Yan measurement where a 190 GeV/c π^- beam impinged on a transversely polarized NH₃ target. The analysis data is from July 8, through November 12 which is after an initial spectrometer and beam commissioning phase. The data is split into 9 periods lasting approximated 2 weeks each, where each period consist of two sub-periods. To reduce systematic effects of acceptance and luminosity dependencies, the NH₃ target was split into two oppositely polarized cells with one cell polarized vertically up and one cell polarized vertically down in the lab frame. The cells were separated by 20 cm and the polarization of both cells was flipped between sub-periods. A summary of the data taking from each period is shown in Table 2.1.

Period	Sub-period	Polarization	First-Last run	Begin date	End date
W07	one	$\downarrow\uparrow$	259363 - 259677	July 9	July 15
	two	$\uparrow\downarrow$	259744 - 260016	July 16	July 22
W08	one	$\uparrow\downarrow$	260074 - 260264	July 23	July 29
	two	$\downarrow\uparrow$	260317 - 260565	July 29	August 5
W09	one	$\downarrow\uparrow$	260627 - 260852	August 5	August 12
	two	$\uparrow\downarrow$	260895 - 261496	August 12	August 26
W10	one	$\uparrow\downarrow$	261515 - 261761	August 26	September 1
	two	$\downarrow\uparrow$	261970 - 262221	September 4	September 9
W11	one	$\downarrow\uparrow$	262370 - 262772	September 11	September 22
	two	$\uparrow\downarrow$	262831 - 263090	September 23	September 30
W12	one	$\uparrow\downarrow$	263143 - 263347	September 30	October 7
	two	$\downarrow\uparrow$	263386 - 263603	October 8	October 14
W13	one	$\downarrow\uparrow$	263655 - 263853	October 15	October 21
	two	$\uparrow\downarrow$	263926 - 264134	October 22	October 28
W14	one	$\uparrow\downarrow$	264170 - 264330	October 28	November 2
	two	$\downarrow\uparrow$	264429 - 264562	November 4	November 8
W15	one	$\downarrow\uparrow$	264619 - 264672	November 9	November 11
	two	$\uparrow\downarrow$	264736 - 264857	November 12	November 16

Table 2.1: COMPASS 2015 data taking periods

2.1.1 Stability Tests

To ensure the data analyzed were recorded during stable beam and spectrometer conditions, stability of the analysis data was performed on a spill-by-spill and run-by-run basis. The data was recorded in runs with a maximum of 200 spills per run and where one spill can have several thousand events.

Bad Spill Analysis

To determine if a given spill is deemed unstable several macro variables were averaged over the spill and compared to neighboring spills. These macro variables were chosen specifically to be sensitive to the general stability conditions of the spectrometer and are listed in the follower enumerated list Table 2.1.1. The starting criteria for an event was two oppositely charged muons where a muon was defined as having crossed 15 radiation lengths of material.

1. number of beam particles divided by the number of events
2. number of beam particles divided by the number of primary vertices
3. number of hits per beam track divided by the number of beam particles
4. number of primary vertices divided by the number of events
5. number of outgoing tracks divided by the number of events
6. number of outgoing particles from a primary vertex divided by the number of primary vertices
7. number of outgoing particle from primary vertex divided by the number of events
8. number of outgoing particles from primary vertex divided by the number of events
9. number of hits from outgoing particles divided by the number outgoing particles
10. number of μ^+ tracks divided by the number of events
11. number of μ^+ tracks from primary vertex divided by the number of events
12. number of μ^- tracks divided by the number of events
13. number of μ^- tracks from primary vertex divided by the number of events
14. $\sum \chi^2$ of outgoing particles divided by the number of outgoing particles
15. $\sum \chi^2$ of all vertices divided by the number of all vertices in an event

16. Trigger rates (LASxLAS, OTxLAS, LASxMT)

If the spectrometer was stable during a spill the average values from the variables in Table ?? are expected to be constant from one spill to the next. To determine if a spill was recorded in unstable conditions the spill of interest is compared with its neighboring 2500 spill occurring before and after in time. If the spill of interest is a specified sigma away from any of the neighboring spills too many times, the spill of interest is marked as a bad spill. If a spill fails this bad spill criteria for any of the macro variables in Table ?? the spill is deemed bad and not included in the analysis. The criteria for the sigma distance and number times a spill crosses this distance to be deemed a bad are different for each data taking period. In addition to checking the nearest spills for each spill, all the spills in a run are marked bad if the run it has less than 10 spills or greater than 70% bad spills. Table 2.1.1 describes the impact of the bad spill analysis on each period.

Bad Run Analysis

The stability of the spectrometer is also verified on run-by-run check in parallel to the spill-by-spill check. The run-by-run analysis compares kinematic distributions and the average of these distributions per run to the same kinematic distributions and averages from the other runs in a given period. The kinematic distributions tested are: x_N , x_π , x_F , q_T , $M_{\mu\mu}$, P_{μ^+} , P_{μ^-} , P_γ , P_{π^-} , and vertex x , y and z positions. The quantities in the run-by-run analysis are expected to influence the asymmetries measured, however their distributions and averages are not expected to have spin-influenced effects from the limited statistics in just a single run. An unbinned-Kolmogorov test (UKT) is performed to compare each distributions. An UKT test is made between all the runs in a given period and a run is marked bad if it is incompatible with most of the runs in a period. The comparison of mean for each distribution from each run is made with the average from a given period. If one of the kinematical variables has an average more than five standard deviations from the average within a period, the run is rejected. The results of the bad spill rejection after having already applied the bad spill rejection are shown in Table 2.1.1.

Table 2.2: Stability analysis rejection percentages

Period	Bad spill rejection	Bad spill and spill rejection
W07	11.79%	17.94%
W08	18.00%	21.19%
W09	14.76%	17.11%
W10	15.88%	17.80%
W11	22.49%	26.14%
W12	12.71%	13.79%
W13	22.32%	22.73%
W14	8.91%	10.70%
W15	3.94%	3.94%

2.1.2 Event Selection

The cuts in the event selection were chosen to ensure the event consisted of two oppositely charged muons, so called dimuons, resulting from a pion collision in the transversely polarized target. The event selection was initial filtered from miniDSTs to μ DSTs using the criteria of at least two muons detected in the spectrometer. The cuts used in this analysis are described in the following enumerated list where the event selection is performed on these μ DSTs and the events used come from the slot1 production. A summary of the number of events remaining after the last cuts is shown in Table 2.3.

1. Two oppositely charged particles from a common best primary vertex. A primary vertex is defined as any vertex with an associated beam particle. In case of multiple common primary vertices the best primary vertex was determined by CORAL tagging the vertex as best primary (PHAST method `PaVertex::IsBestPrimary()`). In the case that CORAL did not tag any of the common vertices as the best primary the vertex with the smallest spatial χ^2 value was used as the best primary vertex.
2. A dimuon trigger fired. A dimuon trigger firing means there are at least two particles in coincidence in this event. The dimuon triggers used were a coincidence between two particles in the large angle spectrometer, LAS-LAS trigger, or a particle in the large angle spectrometer and a particle in the Outer hodoscope in the small angle spectrometer, LAS-Outer trigger. The LAS-Middle trigger was used as a veto on beam decay muons where beam decay muons result from the decay of the beam pion, kaon or anti-proton into a muon. This beam decay muon can then be in coincidence with a positive muon from another decay or strong reaction in the target. The LAS-Middle trigger was used a veto because this trigger was found to have many events resulting from a beam pion decaying to a muon.
3. Both particles are muons. A muon was defined as having crossed 30 radiation lengths of material between the particles first and last measured points. This criteria has been previously determined to be effective at distinguishing between muons and hadrons. In the data production no detectors were used from upstream of the hadron absorber so the absorber is not included in the determination of material crossed.
4. The first measured point for both particles is before 300 cm and the last measured point is after 1500 cm. This cut ensures both particles have positions upstream of the first spectrometer magnet and downstream of the first muon filter.
5. The timing of both muons is defined. This checks that the time relative to the trigger time is determined for both muons so further timing cuts can be performed.

6. Both muons are in time within 5 nanoseconds. This track time for each muon is defined relative to the trigger time as in the previous cut. This cut helps rejected uncorrelated muons.
7. The muon track's spacial reduced χ^2 's are individually less than 10. This cut ensures track quality.
8. A validation that each muon crossed the trigger it was associated as having triggered. This trigger validation cut was performed by extrapolating (PHAST Method PaTrack::Extrapolate()) each muon track back to the hodoscopes it fired and determining if the muon crossed the geometric acceptance of both hodoscopes.
9. The event does not occur in the bad spill or run list. Many tests were performed to test the basic stability of the spectrometer and beam as described in section 2.1.1. The spills placed on the bad spill list were deemed to occur during unstable data taking conditions.
10. The Drell-Yan kinematics are physical. That is x_π and x_N are between 0 and 1 and x_F is between -1 and 1.
11. The transverse momentum of the virtual photon, q_T is between 0.4 and 5.0 GeV/c. The lower limit ensures azimuthal angular resolution is sufficient and the upper cut is minimal and further ensures the kinematic distributions are physically possible.
12. The vertex originated within the z-positions of the transversely polarized target cells defined by the target group ($-294.5 < Z_{\text{vertex}} < -239.3$ for the upstream target or $-219.5 < Z_{\text{vertex}} < -164.3$ cm for the downstream target).
13. The vertex is within the radius of the polarized target measured to be 1.9 cm.

Cuts	W07	W08	W09	W10	W11	W12	W13	W14	W15	WAll
All Data	19410	19184	19654	20707	31371	23563	20561	13154	7697	175301
Good Spills	15947	14899	16217	16895	23041	20184	16026	11796	7422	142427
$0 < x_\pi, x_N < 1, -1 < x_F < 1$	15932	14886	16200	16885	23022	20171	16013	11794	7414	142317
$0.4 < q_T < 5(\text{GeV}/c)$	14342	13385	14609	15239	20667	18101	14365	10588	6636	127932
Z Vertex within NH ₃	4256	4024	4330	4552	6369	5503	4411	3130	2028	38603
Vertex Radius < 1.9cm	4175	3950	4257	4474	6252	5414	4334	3078	1987	37921

Table 2.3: Event selection statistics for this analysis

2.1.3 Binning

The asymmetries are measured in bins of x_N , x_π , x_F , q_T , and $M_{\mu\mu}$. The binning was determined by requiring equal statistics per physics bin. In addition, the asymmetry is determined in an integrated bin using all the

analysis data. The analyzes binning limits are summarized in Table 2.4.

Kinematics	Lowest limit	Upper limit bin 1	Upper limit bin 2	Upper limit bin 3
x_N	0.0	0.13	0.19	1.0
x_π	0.0	0.40	0.56	1.0
x_F	-1.0	0.22	0.41	1.0
q_T (GeV/c)	0.4	0.86	1.36	5.0
$M_{\mu\mu}$ (GeV/c ²)	4.3	4.73	5.50	8.5

Table 2.4: Analysis binning limits

2.2 Extraction of Asymmetries

There are many ways to determine the left-right asymmetry denoted as A_N . The relevant techniques for the 2015 COMPASS setup are described and compared to ensure confidence in the end results. Sec. 2.2.1 starts with a general introduction to the notations and ideas used for all the asymmetry methods.

2.2.1 Geometric Mean

The number of physics counts, N , detected from any particular target can be written as

$$N = L * \sigma * a, \quad (2.1)$$

where L is the luminosity, σ is the cross-section to produce such an event and a is the acceptance. In simple words, the number of counts detected is the number of possible chances for an event to occur times the probability for an event to occur and that the event will be detected. To get spin-dependent counts for the left-right asymmetry, the target, polarization and left or right direction relative to the spin should be included in the counts formula. Generically this can be written

$$N_{\text{target}, \text{Left(Right)}}^{\uparrow(\downarrow)} = a_{\text{target}, \text{spectrometer direction}}^{\uparrow(\downarrow)} * L_{\text{target}}^{\uparrow(\downarrow)} * \sigma_{\text{Left(Right)}}, \quad (2.2)$$

where $\uparrow(\downarrow)$ denotes the target polarization, target is either the upstream or downstream target Left(Right) is left or right of the spin direction and $\text{spectrometer direction}$ denotes which side of the spectrometer the event was detected on and can be either the Jura or Saleve side.

The previous definitions of the detected counts all depend on the spectrometer acceptance. This is a problem because the spectrometer acceptance can change with time and space and therefore can be dependent on the physical kinematics which produced the event. Such dependences can cause unphysical

false asymmetries in the measurement of A_N and must therefore be removed or must be included as systematic effects.

The geometric mean asymmetry method is a way to determine the left-right asymmetry without acceptance effects from the spectrometer. It is defined as

$$P \frac{\sqrt{N_{\text{up(down)stream, Left}}^{\uparrow} N_{\text{up(down)stream, Left}}^{\downarrow}} - \sqrt{N_{\text{up(down)stream, Right}}^{\uparrow} N_{\text{up(down)stream, Right}}^{\downarrow}}}{\sqrt{N_{\text{up(down)stream, Left}}^{\uparrow} N_{\text{up(down)stream, Left}}^{\downarrow}} + \sqrt{N_{\text{up(down)stream, Right}}^{\uparrow} N_{\text{up(down)stream, Right}}^{\downarrow}}}, \quad (2.3)$$

where P represents the fraction of polarized partons.

Equation 2.3 can be thought of simply as the normalized difference of left minus right counts. Left and right counts are determined relative to the target spin and are defined as

$$\begin{aligned} \text{Left} : \hat{q}_T \cdot (\hat{S}_T \times \hat{P}_\pi) &> 0 \\ \text{Right} : \hat{q}_T \cdot (\hat{S}_T \times \hat{P}_\pi) &< 0, \end{aligned} \quad (2.4)$$

where \hat{q}_T , \hat{S}_T and \hat{P}_π are unit vectors in the target reference frame for the virtual photon transverse momentum, the target spin and the beam pion momentum respectively.

Using Eq. 2.2 for the definition of counts, the geometric mean asymmetry is

$$P \frac{\kappa \sqrt{\sigma_{\text{Left}} \sigma_{\text{Left}}} - \sqrt{\sigma_{\text{Right}} \sigma_{\text{Right}}}}{\kappa \sqrt{\sigma_{\text{Left}} \sigma_{\text{Left}}} + \sqrt{\sigma_{\text{Right}} \sigma_{\text{Right}}}}, \quad (2.5)$$

where κ is a ratio of acceptances defined as

$$\kappa_{\text{geomean}} = \frac{\sqrt{a_{\text{up(down)stream, Jura}}^{\uparrow} a_{\text{up(down)stream, Saleve}}^{\downarrow}}}{\sqrt{a_{\text{up(down)stream, Saleve}}^{\uparrow} a_{\text{up(down)stream, Jura}}^{\downarrow}}}. \quad (2.6)$$

Here the detection side of spectrometer is specified by looking down the beam line as either Jura to mean left or Saleve to mean right. These relations of Jura is left and Saleve is right are only strictly true if the target polarization is pointing straight up or straight down in the target frame. In particular if the beam particle and the target polarization do not make a right angle in the laboratory frame this relation will no longer be strictly true but is an approximation for ease of notation.

Relation 2.5 is equal to A_N if κ is equal to one. However as stated previously, time effects can vary κ from unity. These effects are estimated through false asymmetry analysis and included in the systematics. Equation 2.3 is therefore to a good approximation an acceptance free method to determine A_N . It is also defined for the upstream and downstream targets independently and therefore can be used as a consistency

check between the two targets.

The statistical uncertainty of the geometry mean is

$$\frac{1}{P} \frac{\sqrt{N_{\text{Left}}^{\uparrow} N_{\text{Left}}^{\downarrow} N_{\text{Right}}^{\uparrow} N_{\text{Right}}^{\downarrow}}}{\left(\sqrt{N_{\text{Left}}^{\uparrow} N_{\text{Left}}^{\downarrow}} + \sqrt{N_{\text{Right}}^{\uparrow} N_{\text{Right}}^{\downarrow}} \right)^2} \sqrt{\frac{1}{N_{\text{Left}}^{\uparrow}} + \frac{1}{N_{\text{Left}}^{\downarrow}} + \frac{1}{N_{\text{Right}}^{\uparrow}} + \frac{1}{N_{\text{Right}}^{\downarrow}}} , \quad (2.7)$$

which reduces to $\frac{1}{P} \frac{1}{\sqrt{N}}$ in the case of equal statistics in each direction and polarization.

2.2.2 Two Target Geometric Mean

The previous method determined an A_N per target and as mentioned before COMPASS had two oppositely polarized targets in 2015. It would therefore make sense from a statistical point of view and for comparison purposes to determine A_N using all the information from the 2015 COMPASS setup. This can be accomplished by modifying the geometric mean to add both targets as follows

$$\frac{1}{P} \frac{\sqrt[4]{N_{\text{up},\text{Left}}^{\uparrow} N_{\text{up},\text{Left}}^{\downarrow} N_{\text{down},\text{Left}}^{\uparrow} N_{\text{down},\text{Left}}^{\downarrow}} - \sqrt[4]{N_{\text{up},\text{Right}}^{\uparrow} N_{\text{up},\text{Right}}^{\downarrow} N_{\text{down},\text{Right}}^{\uparrow} N_{\text{down},\text{Right}}^{\downarrow}}}{\sqrt[4]{N_{\text{up},\text{Left}}^{\uparrow} N_{\text{up},\text{Left}}^{\downarrow} N_{\text{down},\text{Left}}^{\uparrow} N_{\text{down},\text{Left}}^{\downarrow}} + \sqrt[4]{N_{\text{up},\text{Right}}^{\uparrow} N_{\text{up},\text{Right}}^{\downarrow} N_{\text{down},\text{Right}}^{\uparrow} N_{\text{down},\text{Right}}^{\downarrow}}}, \quad (2.8)$$

where up and down stand for the upstream and downstream targets respectfully.

As in the basic geometric mean, left and right are determined relative to the spin direction of the target as in Eq. 2.4. Again using Eq. 2.2 for the definition of counts, the two target geometric mean asymmetry, Eq. 2.8, can be written as

$$\frac{1}{P} \frac{\kappa \sqrt[4]{\sigma_{\text{Left}} \sigma_{\text{Left}} \sigma_{\text{Left}} \sigma_{\text{Left}}} - \sqrt[4]{\sigma_{\text{Right}} \sigma_{\text{Right}} \sigma_{\text{Right}} \sigma_{\text{Right}}}}{\sqrt[4]{\sigma_{\text{Left}} \sigma_{\text{Left}} \sigma_{\text{Left}} \sigma_{\text{Left}}} + \sqrt[4]{\sigma_{\text{Right}} \sigma_{\text{Right}} \sigma_{\text{Right}} \sigma_{\text{Right}}}}, \quad (2.9)$$

,

where now κ is the ratio of acceptances from all targets and polarizations. This all inclusive acceptance ratio is defined as

$$\kappa_{\text{two-target}} = \frac{\sqrt[4]{a_{\text{up,Jura}}^{\uparrow} a_{\text{up,Saleve}}^{\downarrow} a_{\text{down,Jura}}^{\uparrow} a_{\text{down,Saleve}}^{\downarrow}}}{\sqrt[4]{a_{\text{up,Saleve}}^{\uparrow} a_{\text{up,Jura}}^{\downarrow} a_{\text{down,Saleve}}^{\uparrow} a_{\text{down,Jura}}^{\downarrow}}}. \quad (2.10)$$

In this case the acceptance ratio is expected to vary less with time and therefore be closer to unity than the normal geometric mean acceptance ratio, Eq. 2.6. This is a consequence of having the different target cells oppositely polarized. Rewriting Eq. 2.10 with sub-period superscripts instead of target polarization superscripts

$$\kappa_{two-target} = \frac{\sqrt[4]{a_{up,Jura}^a a_{up,Saleve}^b a_{down,Jura}^b a_{down,Saleve}^a}}{\sqrt[4]{a_{up,Saleve}^a a_{up,Jura}^b a_{down,Saleve}^b a_{down,Jura}^a}}, \quad (2.11)$$

where sub-period a is with the upstream target polarized up and the downstream target polarized down and vice versa for sub-period b . From Eq. 2.11 it is more evident that the acceptance ratio terms for sub-period b are reciprocal to the terms for sub-period a and therefore the acceptance ratio is expected to be more stably close to unity.

Finally the statistical uncertainty of the two target geometric mean is

$$\frac{1}{P} \frac{LR}{(L+R)^2} \sqrt{\sum_{\text{target polarization}} \left(\frac{1}{N_{\text{target},\text{Left}}^{\text{polarization}}} + \frac{1}{N_{\text{target},\text{Right}}^{\text{polarization}}} \right)}, \quad (2.12)$$

where L can be thought of as the left counts and equals to $\sqrt[4]{N_{up,\text{Left}}^{\uparrow} N_{up,\text{Left}}^{\downarrow} N_{down,\text{Left}}^{\uparrow} N_{down,\text{Left}}^{\downarrow}}$ and R can be thought of as the right counts and equals $\sqrt[4]{N_{up,\text{Right}}^{\uparrow} N_{up,\text{Right}}^{\downarrow} N_{down,\text{Right}}^{\uparrow} N_{down,\text{Right}}^{\downarrow}}$. The statistical uncertainty for the two target geometric mean also reduces to $\frac{1}{P} \frac{1}{\sqrt{N}}$ in the case of equal statistics in each direction and polarization.

2.3 Systematic Studies

Several tests were performed to estimate the systematic uncertainty. The systematic errors are determined by adding all non-zero systematic effects in quadrature. The impact from each source of systematic error is summarized in Tab. 2.7.

2.3.1 Period Compatibility

The asymmetries calculated for each period in each kinematic bin are shown in Fig. 2.1.

By eye the asymmetry fluctuations appear to be statistically compatible. To quantify the compatibility of the asymmetries between the periods, a pull distribution is formed. The pull value is defined as

$$\Delta A_i = \frac{A_i - \langle A \rangle}{\sqrt{\sigma_{A_i}^2 - \sigma_{\langle A \rangle}^2}}, \quad (2.13)$$

and is determined for each period and kinematic bin. There are therefore $3(\text{number of bins}) \times 5(\text{number of kinematics}) \times 9(\text{number of periods}) = 135$ entries in the pull distribution. This distribution is shown in Fig. 2.2 along with a Gaussian fit. If the asymmetries all come from the same parent distribution then

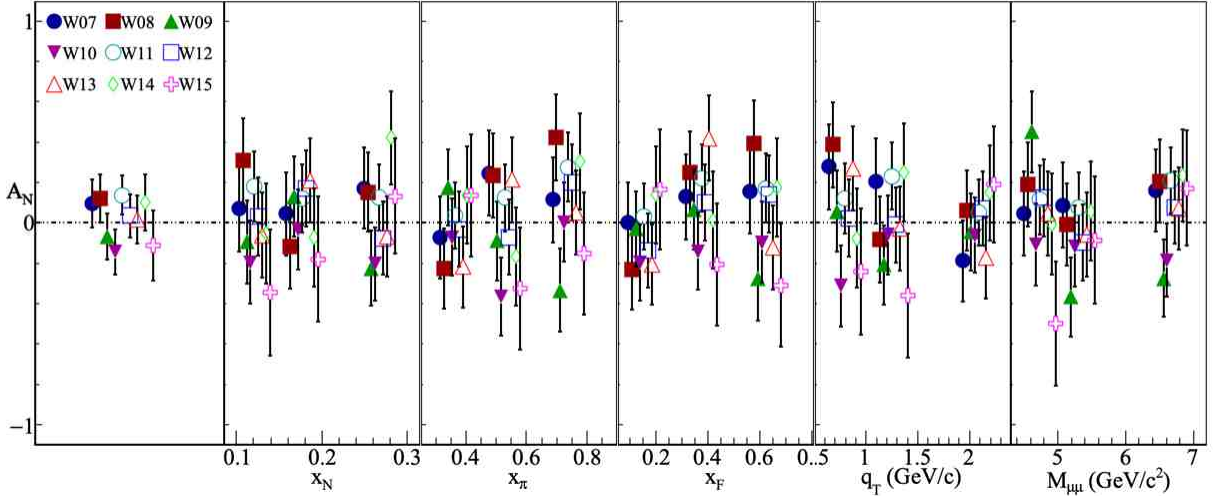


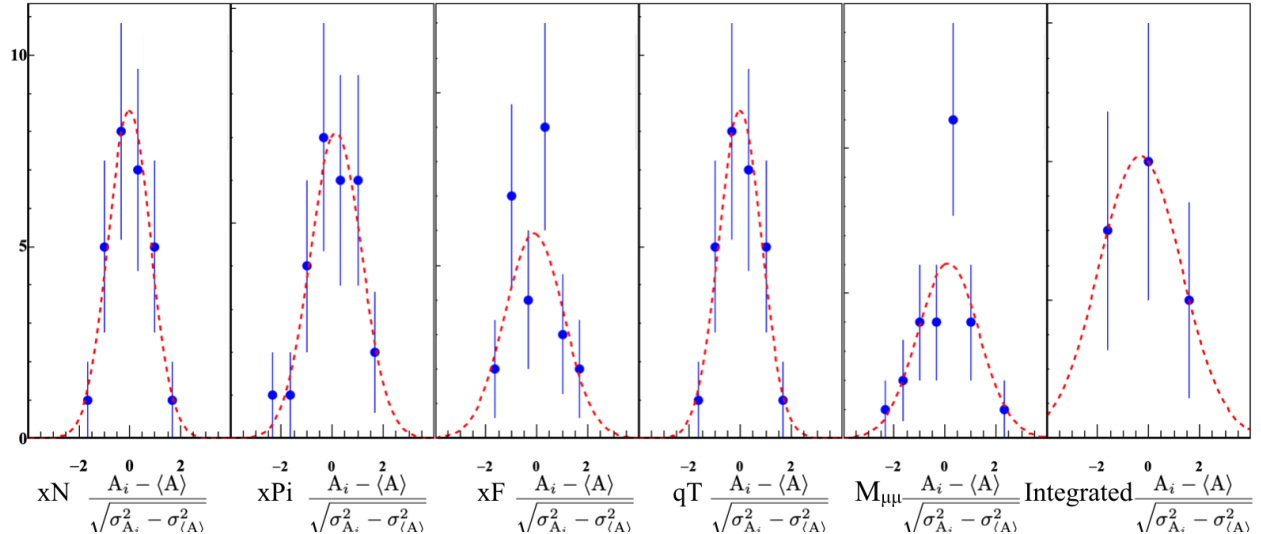
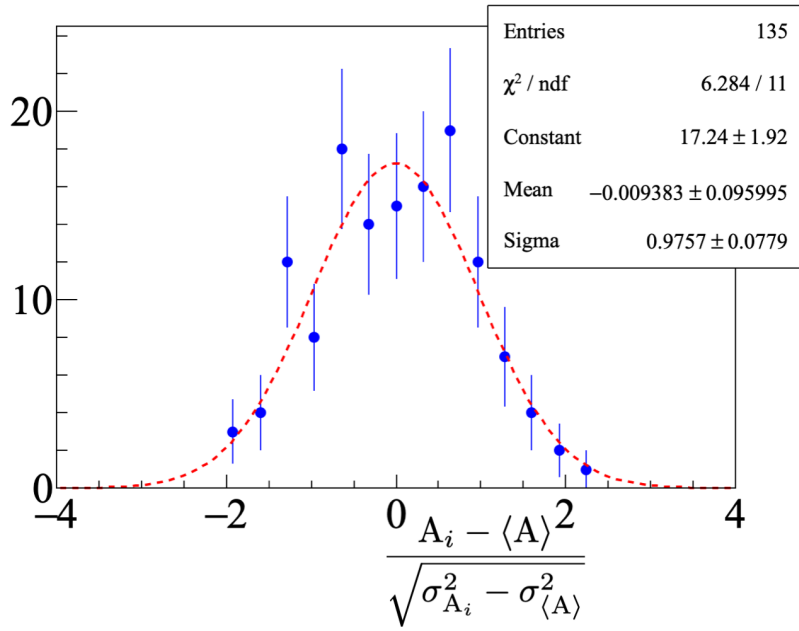
Figure 2.1: A_N determined for each period

due to the central limit theorem the pull distribution will be a Gaussian distribution with zero mean and unit variance. The discrepancy of the pull distribution from a standard Gaussian distribution is used to determine a systematic error as

$$\frac{\sigma_{\text{systematic}}}{\sigma_{\text{statistical}}} = \sqrt{|\sigma_{\text{pull}}^2 - 1|} + \frac{\mu_{\text{pull}}}{2}. \quad (2.14)$$

As the asymmetries in different kinematic bins are formed using the same data set the asymmetries between kinematics are correlated. For this reason an uncorrelated pull distribution is also formed for each physics kinematic bin and also compared with a standard Gaussian distribution. These distributions are shown in Fig. 2.3 and the results of the Gaussian fit are shown in Fig. 2.4. For these uncorrelated pull distributions there are now only $3(\text{number of bins}) \times 9(\text{number of periods}) = 27$ entries in each kinetically binned pull distributions and only $9(\text{number of periods})$ bins in the integrated pull distribution.

Even though the Gaussian fits did not give exactly as standard Gaussian, the fit parameters well compatible with a standard Gaussian within the errors of the fit. Therefore no systematic error was assigned due to incompatibility of the periods.



Entries	27	Entries	27	Entries	27	Entries	27	Entries	27	Entries	9
χ^2 / ndf	0.4347 / 3	χ^2 / ndf	1.056 / 4	χ^2 / ndf	3.416 / 3	χ^2 / ndf	0.4347 / 3	χ^2 / ndf	3.152 / 4	χ^2 / ndf	1.091e-08 / 0
Constant	8.548 ± 2.043	Constant	7.101 ± 1.827	Constant	5.922 ± 1.622	Constant	8.548 ± 2.043	Constant	6.038 ± 1.603	Constant	4.085 ± 1.992
Mean	-0.01562 ± 0.17221	Mean	0.1422 ± 0.2204	Mean	-0.1036 ± 0.2910	Mean	-0.01562 ± 0.17221	Mean	0.1287 ± 0.2860	Mean	-0.3308 ± 0.8192
Sigma	0.8386 ± 0.1304	Sigma	1.004 ± 0.201	Sigma	1.15 ± 0.31	Sigma	0.8386 ± 0.1304	Sigma	1.197 ± 0.256	Sigma	1.616 ± 1.101

Figure 2.4: Results of Gaussian fit for the uncorrelated pull distributions

2.3.2 False Asymmetries

Acceptance From False Asymmetries

As was pointed out in Sec. 2.2.1 and Sec. 2.2.2, the asymmetry measurement assumes the acceptance does not change with time and therefore the acceptance ratios Eq. 2.6 and Eq. 2.10 are unitary. Any deviation from a unitary acceptance ratio is estimated with a false asymmetry and the errors are included as systematic errors. To determine if acceptance does change with time, a false asymmetry is calculated where the only way the false asymmetry could be non-zero is if acceptance changes with time. This false asymmetry for the two target geometric mean is

$$A_{N,\text{False}} = \frac{1}{P} \frac{\sqrt[4]{N_{\text{up},\text{Right}}^\uparrow N_{\text{up},\text{Left}}^\downarrow N_{\text{down},\text{Left}}^\uparrow N_{\text{down},\text{Right}}^\downarrow} - \sqrt[4]{N_{\text{up},\text{Left}}^\uparrow N_{\text{up},\text{Right}}^\downarrow N_{\text{down},\text{Right}}^\uparrow N_{\text{down},\text{Left}}^\downarrow}}{\sqrt[4]{N_{\text{up},\text{Right}}^\uparrow N_{\text{up},\text{Left}}^\downarrow N_{\text{down},\text{Left}}^\uparrow N_{\text{down},\text{Right}}^\downarrow} + \sqrt[4]{N_{\text{up},\text{Left}}^\uparrow N_{\text{up},\text{Right}}^\downarrow N_{\text{down},\text{Right}}^\uparrow N_{\text{down},\text{Left}}^\downarrow}} \quad (2.15)$$

$$= \frac{1}{P} \frac{\alpha \sqrt[4]{\sigma_{\text{Right}} \sigma_{\text{Left}} \sigma_{\text{Left}} \sigma_{\text{Right}}} - \sqrt[4]{\sigma_{\text{Left}} \sigma_{\text{Right}} \sigma_{\text{Right}} \sigma_{\text{Left}}}}{\alpha \sqrt[4]{\sigma_{\text{Right}} \sigma_{\text{Left}} \sigma_{\text{Left}} \sigma_{\text{Right}}} + \sqrt[4]{\sigma_{\text{Left}} \sigma_{\text{Right}} \sigma_{\text{Right}} \sigma_{\text{Left}}}}$$

$$= \frac{1}{P} \frac{\alpha - 1}{\alpha + 1}, \quad (2.16)$$

where α is an acceptance ratio and is defined as

$$\frac{\sqrt[4]{a_{\text{up}, \text{Saleve}}^{\uparrow} a_{\text{up}, \text{Saleve}}^{\downarrow} a_{\text{down}, \text{Jura}}^{\uparrow} a_{\text{down}, \text{Jura}}^{\downarrow}}}{\sqrt[4]{a_{\text{up}, \text{Jura}}^{\uparrow} a_{\text{up}, \text{Jura}}^{\downarrow} a_{\text{down}, \text{Saleve}}^{\uparrow} a_{\text{down}, \text{Saleve}}^{\downarrow}}}. \quad (2.17)$$

The false asymmetry, Eq. 2.15, can be simplified as

$$A_{N,\text{False}} = \frac{1}{P} \frac{\sqrt[4]{N_{\text{up}, \text{Saleve}} N_{\text{down}, \text{Jura}}} - \sqrt[4]{N_{\text{up}, \text{Jura}} N_{\text{down}, \text{Saleve}}}}{\sqrt[4]{N_{\text{up}, \text{Saleve}} N_{\text{down}, \text{Jura}}} + \sqrt[4]{N_{\text{up}, \text{Jura}} N_{\text{down}, \text{Saleve}}}}. \quad (2.18)$$

That is $A_{N,\text{false}}$ is the normalized difference of counts from each target cell assuming the upstream target is always polarized down and the downstream target is always polarized up. Given that the polarization flips for both upstream and downstream target cells, $A_{N,\text{false}}$ is an asymmetry where physical effects cancel out. The kinematic dependencies of the false asymmetry are shown in Fig. 2.5 and the kinematic dependencies of the acceptance ratio, α , are shown in Fig. 2.6.

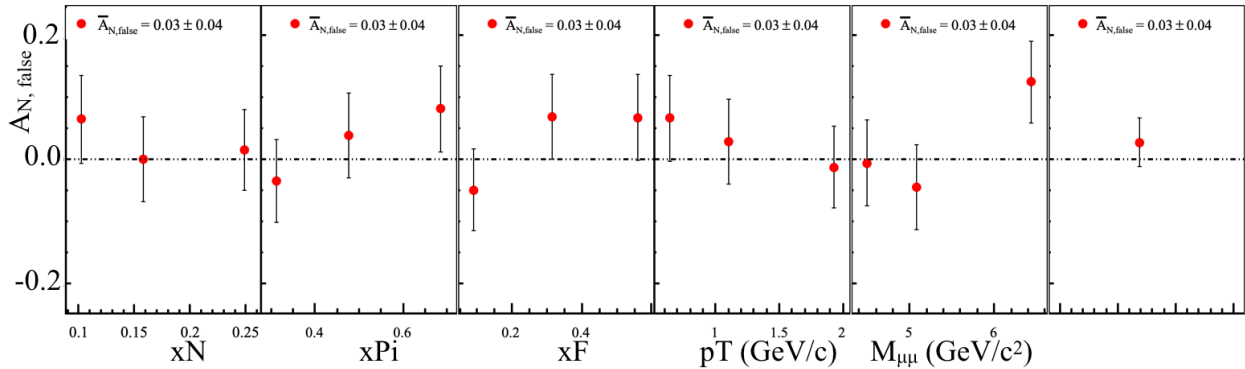


Figure 2.5: False asymmetry to estimate fluctuations in acceptance in time

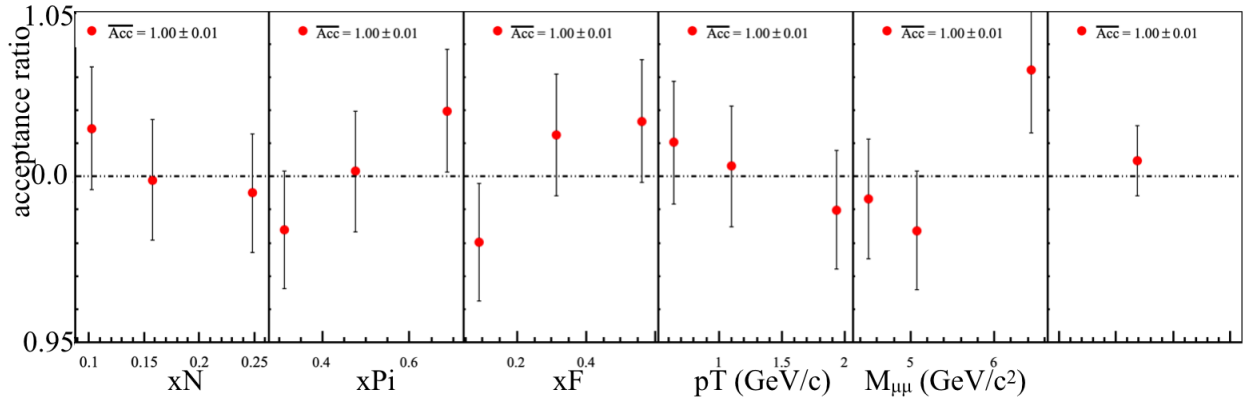


Figure 2.6: Acceptance ratio used to determine the systematic effects from acceptance changes in time

While α is an acceptance ratio it is not the same as the acceptance ratio in the true asymmetry. However α is similar to the true acceptance ratio, κ , in that α will only be different from unity as a result of time changes in the spectrometer. Therefore it is assumed α can be used as a good estimate of the true acceptance ratio fluctuations. The systematic error due to acceptance fluctuations is determined as

$$\delta A_{N,\text{systematic}} = \frac{1}{P} \left(\frac{|\alpha - 1|}{2} + \delta_{\frac{|\alpha - 1|}{2}} \right), \quad (2.19)$$

where this expression is derived in Appendix A.1. The kinematic dependence of the systematic error normalized to the statistical error is shown in Fig. 2.7. The binned average systematic error due to acceptance is 20% of the statistical error.

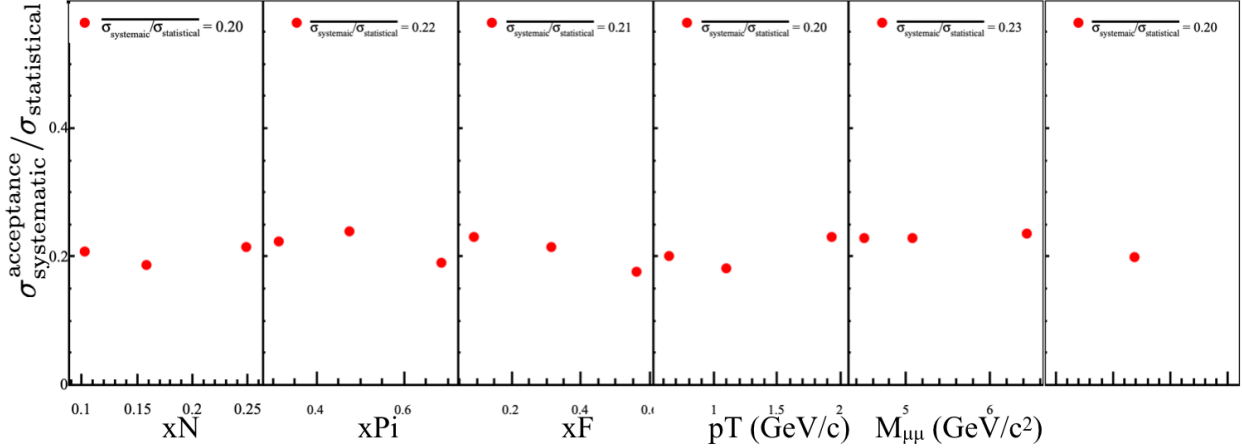


Figure 2.7: Systematic error due to acceptance effects

2.3.3 Further False Asymmetry Effects

Although the list of systematic effects specifically studied is quite exhaustive there is always the potential for other systematic effects not considered. Studies of the changes in time from additional false asymmetries were performed in an attempt to take into account all other systematic effects. All false asymmetries considered must be constructed in such a way that the physical process of interest cancels out. A false asymmetry could therefore only be non-zero from acceptance effects, luminosity or some other reason not considered. The additional false asymmetries constructed are made in a way that luminosity effects canceled out and acceptance effects were approximately constant. With these assumptions pull values from Eq. 2.13 should be distributed as a standard Gaussian distribution. Any deviation from a standard Gaussian is con-

servatively taken as a systematic effect from some unknown cause. The additional studied false asymmetries are summarized in the following enumerated list.

1. A false asymmetry similar to Eq. 2.15 but with the upstream left and right counts flipped defined as

$$\frac{1}{P} \frac{\sqrt[4]{N_{\text{up},\text{Left}}^{\uparrow} N_{\text{up},\text{Right}}^{\downarrow} N_{\text{down},\text{Left}}^{\uparrow} N_{\text{down},\text{Right}}^{\downarrow}} - \sqrt[4]{N_{\text{up},\text{Right}}^{\uparrow} N_{\text{up},\text{Left}}^{\downarrow} N_{\text{down},\text{Right}}^{\uparrow} N_{\text{down},\text{Left}}^{\downarrow}}}{\sqrt[4]{N_{\text{up},\text{Left}}^{\uparrow} N_{\text{up},\text{Right}}^{\downarrow} N_{\text{down},\text{Left}}^{\uparrow} N_{\text{down},\text{Right}}^{\downarrow}} + \sqrt[4]{N_{\text{up},\text{Right}}^{\uparrow} N_{\text{up},\text{Left}}^{\downarrow} N_{\text{down},\text{Right}}^{\uparrow} N_{\text{down},\text{Left}}^{\downarrow}}} \quad (2.20)$$

This false asymmetry can be thought of as measuring the normalized counts on the Jura side minus the Saleve side. The period weighted average results of this false asymmetry are shown in Fig. 2.8 and as can be seen there is the asymmetry is systematically less than zero by more than a standard deviation. The uncorrelated pull distributions from this false asymmetry are shown in Fig. 2.9 and the corresponding Gaussian fit results are shown in Fig. 2.10. Due to the fact that there are less entries in these pull distributions the Gaussian fit results are not necessarily that good. In an attempt to correct for this and to take into account the fit errors, a weighted average of the mean and standard deviation are made, as in Eq. 2.24, using weights as the inverse fit variances. The resulting systematic error is again determined as in Eq. 2.14 using the weighted mean and weighted standard deviation.

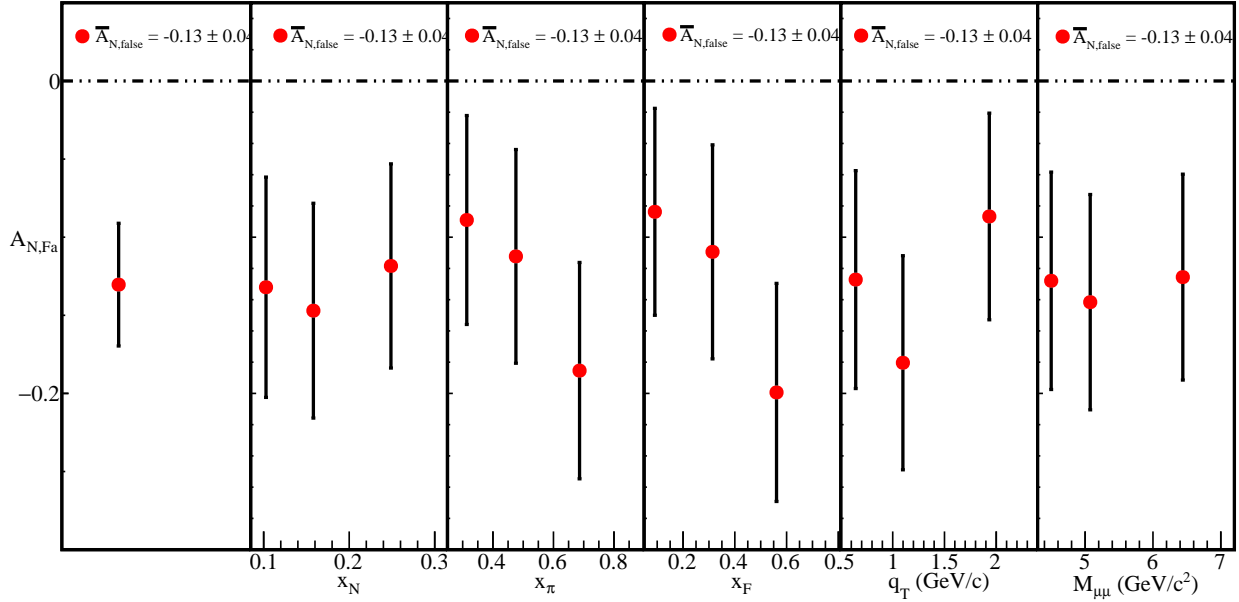


Figure 2.8: Two target geometric false asymmetry. This is non-zero due to acceptance effects

2. A false asymmetries using only the information from the upstream or the downstream target defined as

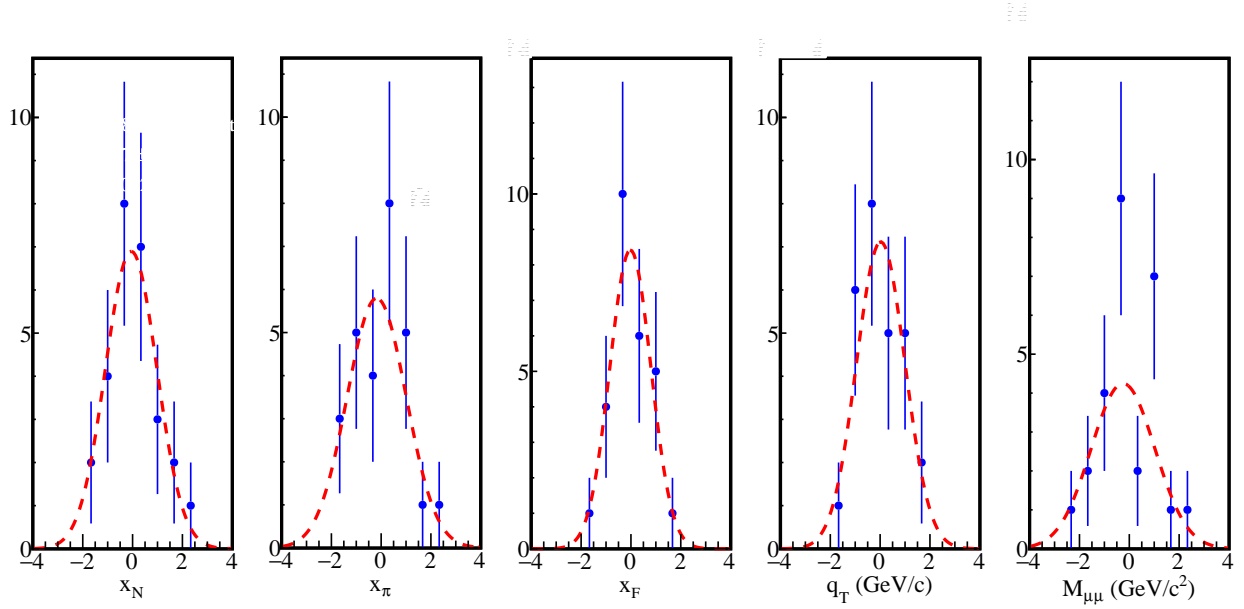


Figure 2.9: Uncorrelated pulls of the two target geomean false asymmetry

Entries	27	Entries	27	Entries	27	Entries	27	Entries	27
χ^2 / ndf	1.06 / 4	χ^2 / ndf	2.875 / 4	χ^2 / ndf	1.203 / 3	χ^2 / ndf	1.925 / 3	χ^2 / ndf	7.364 / 5
Constant	6.898 ± 2.019	Constant	5.797 ± 1.578	Constant	8.419 ± 2.089	Constant	7.116 ± 1.826	Constant	4.248 ± 1.307
Mean	-0.05617 ± 0.22189	Mean	-0.1796 ± 0.3545	Mean	-0.02243 ± 0.17361	Mean	0.0256 ± 0.2382	Mean	-0.2528 ± 0.3265
Sigma	1.032 ± 0.266	Sigma	1.187 ± 0.317	Sigma	0.8256 ± 0.1377	Sigma	0.9721 ± 0.1962	Sigma	1.279 ± 0.331

Figure 2.10: Gaussian git results for the uncorrelated two target false geomean pulls

$$\frac{1}{P} \frac{\sqrt{N_{\text{up(down)stream,Left}}^{\uparrow} N_{\text{up(down)stream,Right}}^{\downarrow}} - \sqrt{N_{\text{up(down)stream,Right}}^{\uparrow} N_{\text{up(down)stream,Left}}^{\downarrow}}}{\sqrt{N_{\text{up(down)stream,Left}}^{\uparrow} N_{\text{up(down)stream,Right}}^{\downarrow}} + \sqrt{N_{\text{up(down)stream,Right}}^{\uparrow} N_{\text{up(down)stream,Left}}^{\downarrow}}}. \quad (2.21)$$

This false asymmetry can also be thought of as measuring the normalized counts on the Jura side minus the Saleve side but for each target individually. Both this false asymmetry and the previous false asymmetry can be written as Eq. 2.16 where α will be an acceptance ratio of Jura/Saleve.

As the Jura/Saleve acceptance ratio is expected to be the same for the upstream and downstream targets, any difference between the two false asymmetries must be due to other reasons. A by period comparison between the upstream and downstream target is shown in Fig. 2.11 and as can be seen there are differences by period between the upstream and downstream asymmetries. A combined pull distribution is made using the information from both upstream and downstream asymmetries and is shown in Fig. 2.12. As with the previous false asymmetry, lack of data leads to the same problems with fit and therefore the same weighting method is used to determine a systematic error.

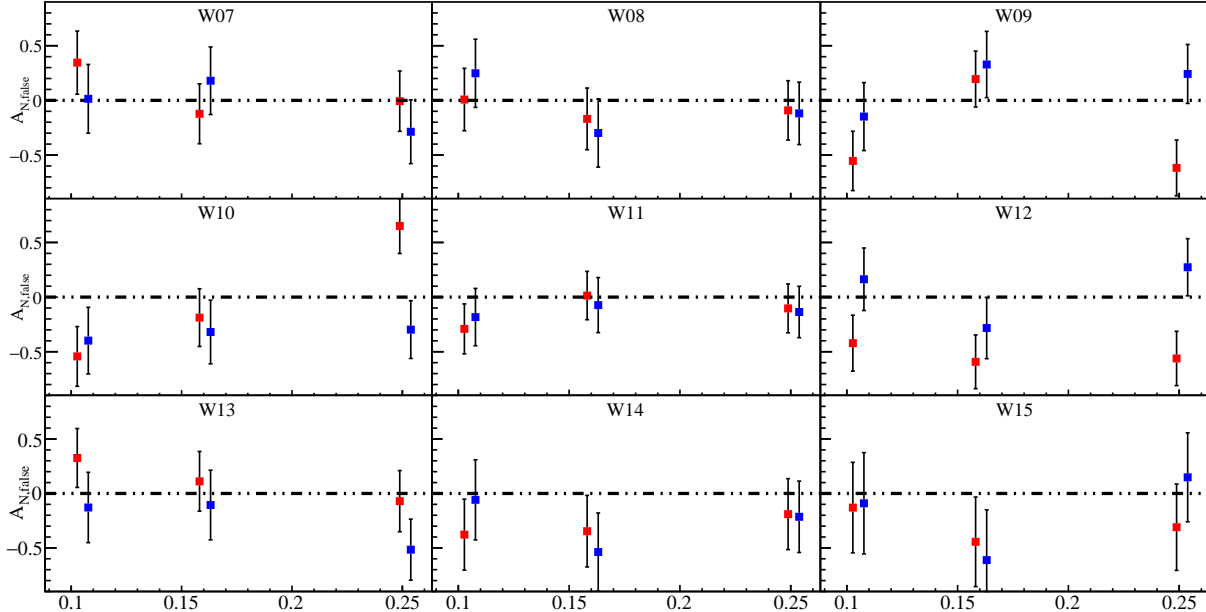


Figure 2.11: One target false asymmetries for the upstream target (red) and the downstream target (blue), as a function of x_N . Each graph is from a different period in time.

3. Finally the same false asymmetry used to determine the acceptance fluctuations, Eq. 2.15, is also checked for compatibility and a systematic error is determined in the same way as the previous false asymmetries. The pulls are shown in Fig. 2.13 and the corresponding fit parameters are shown in Fig. 2.14.

A summary of the systematic error from each false asymmetry is shown in Tab. 2.5

2.3.4 Left/Right Event Migration

The spectrometer has finite resolution for any measured quantity and for this reason events measured as left outgoing could really be events that are right outgoing and vice versa for measured left outgoing events. This left-right miss-identification has the result of diluting spin-dependent effects by effectively having a sample

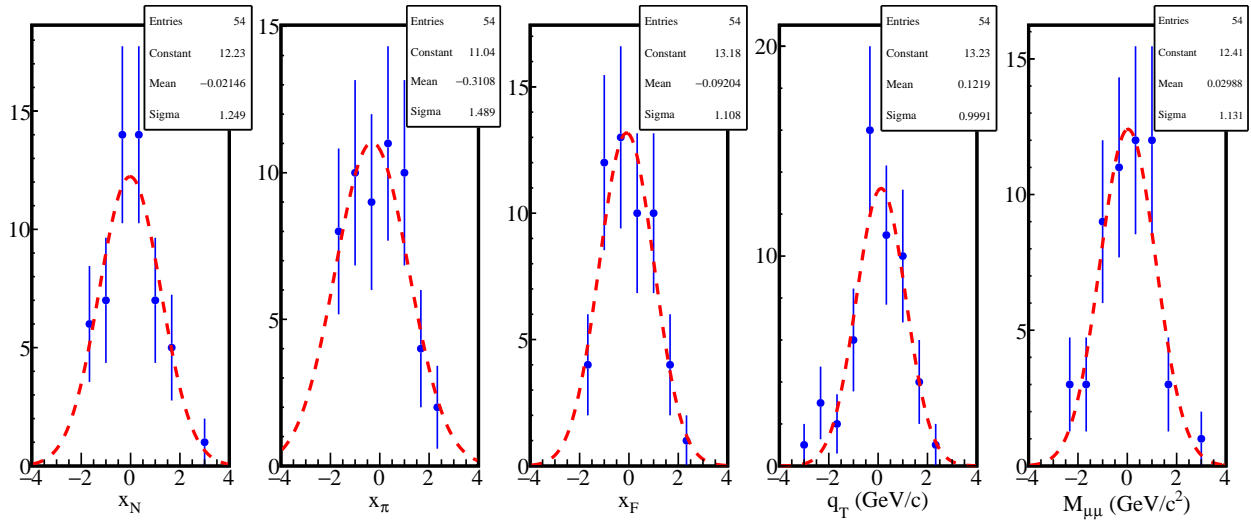


Figure 2.12: Pull values from one target geomean false asymmetries. Both upstream and downstream values are used to make this pull

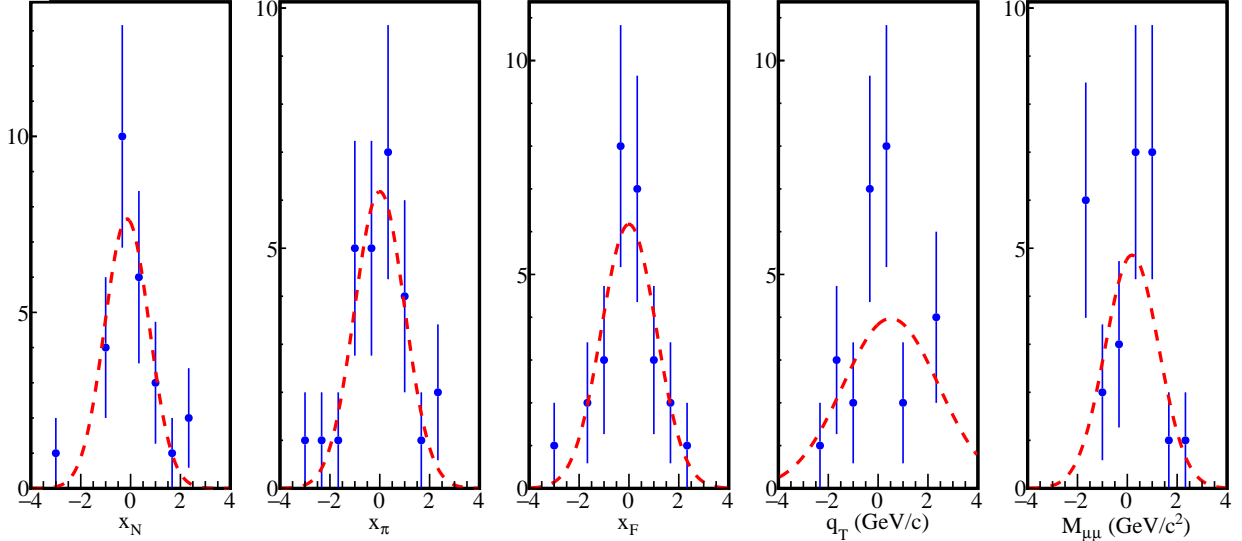


Figure 2.13: Pull distribution for a nearly acceptance free two target false geomean asymmetry

Systematic error	$\langle \sigma_{\text{systematic}} / \sigma_{\text{statistical}} \rangle$
Two target Jura-Saleve	0.26
Combined one target	0.5
Two target acceptance estimation	0.29

Table 2.5: Summary of systematic error impacts from false asymmetries. The maximum systematic error is chosen as the systematic error.

Entries	27	Entries	27	Entries	27	Entries	27	Entries	27
χ^2 / ndf	3.517 / 4	χ^2 / ndf	3.737 / 6	χ^2 / ndf	2.357 / 5	χ^2 / ndf	6.734 / 4	χ^2 / ndf	7.973 / 4
Constant	7.658 ± 3.014	Constant	6.183 ± 1.859	Constant	6.176 ± 2.115	Constant	3.971 ± 1.201	Constant	4.857 ± 4.667
Mean	-0.1441 ± 0.2765	Mean	-0.002351 ± 0.211941	Mean	-0.002406 ± 0.246275	Mean	0.5095 ± 1.1086	Mean	0.1882 ± 0.9446
Sigma	0.891 ± 0.424	Sigma	1.004 ± 0.226	Sigma	1.098 ± 0.361	Sigma	1.92 ± 1.12	Sigma	1.072 ± 1.195

Figure 2.14: Gaussian fit results for the previous pull distributions

from an unpolarized target along with the sample from the polarized target. Therefore the asymmetry A_N reduces from left-right miss-identification and this effect is included as a systematic effect.

For this thesis five Monte-Carlo processes were generated corresponding to three background processes and a spin-independent signal process. The generated used was PHTHYIA8 and the data was generated and reconstruction at Blue Waters. The background processes simulated were JPs ψ production, Ps ψ' production and open charm (OC) production. Each of these backgrounds can decay into two muons which results in a background contamination to the Drell-Yan signal. Table 2.3.4 gives the parameters used for the Monte-Carlo studied.

Table 2.6: Monte-Carlo settings produced on Blue Waters

Event generator	PYTHIA8
Pion pdf	GRVPII
Proton pdf	NNPDF23
proton/neutron mixing ratio	1.96
Initial state radiation	on
Final state radiation	on
Multiple parton interactions	on
Simulated detector efficiencies	uniform

Miss-identification was estimated from the simulated Monte-Carlo data sample described in Table 2.3.4 where the sample was made from the respond of the COMPASS spectrometer to input Drell-Yan events in a similar mass range. The same analysis performed on real data was performed on this Monte-Carlo data to get the angles of interest. Fig. 2.15 shows the rate of events identified correctly and incorrectly as a function of the ϕ_S . This plot is made by determining which outgoing direction the generated events emerged with

the outgoing direction the reconstructed events emerged.

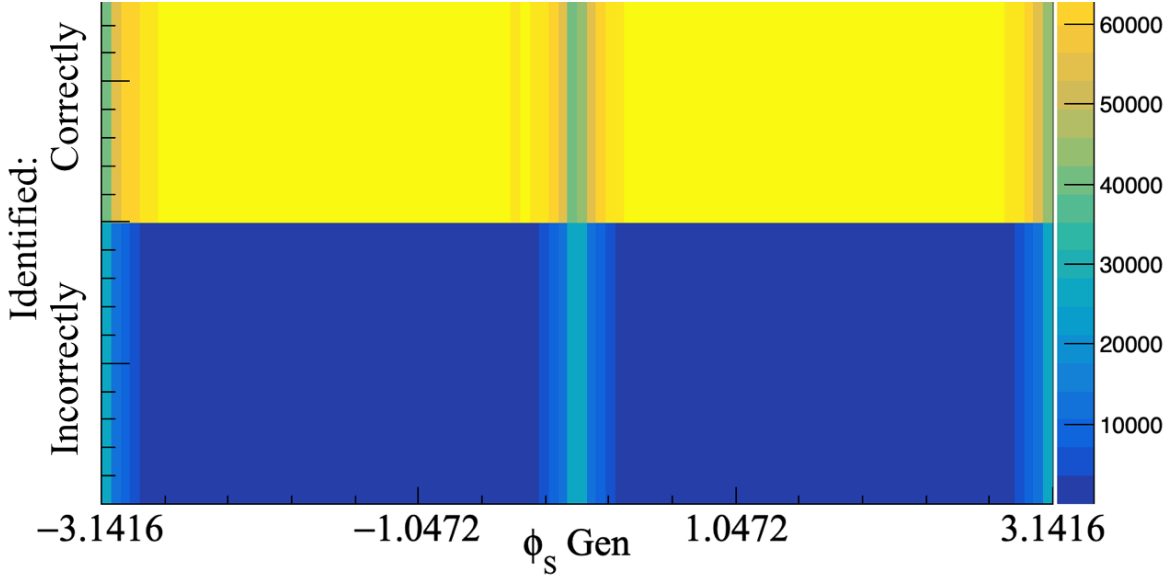


Figure 2.15: The rate of identified correctly and incorrectly left-right events as a function of ϕ_S . This is determined by comparing the generated outgoing direction with the reconstructed outgoing direction. The left-right boundary is clearly visible at 0° and $-\pi^\circ$ and π°

As is clearly visible there is a band of higher miss-identification rate at the border between left and right.

For this reason a cut in the ϕ_S variable symmetric about the left-right border was tested to determine the percent of miss-identification as a function of the amount of ϕ_S cut. These results are shown in Fig. 2.16.

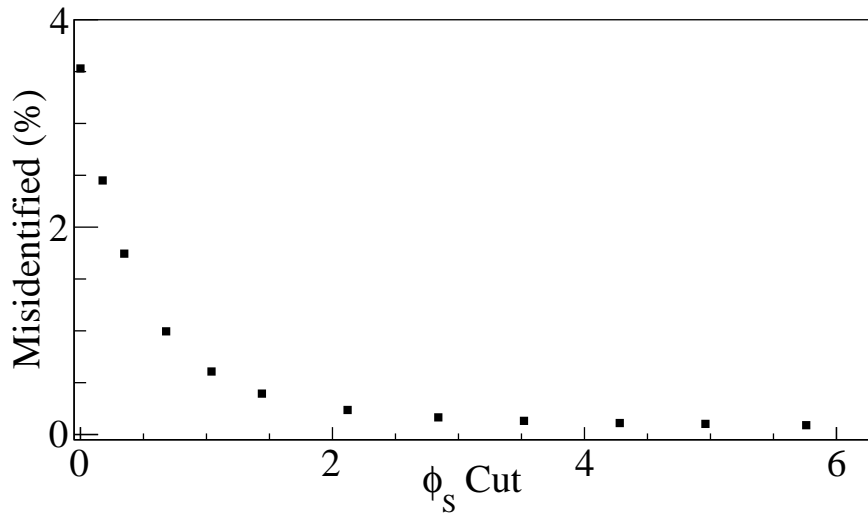


Figure 2.16: Percent left-right migration as a function of the amount of ϕ_S cut.

The systematic error for left-right migration is calculated as

$$\delta A_{N,\text{systematic}} = \gamma * A_N + \gamma * \delta A_N, \quad (2.22)$$

where this expression is derived in Appendix A.2.

No cut on ϕ_S was used for the asymmetry due to the fact that the systematic error is already small with no cut in ϕ_S and to avoid loss of statistics. The integrated systematic error due to left-right event migration was determined to be 9%.

2.3.5 Total Systematics

The total systematic error is determined by adding all non-zero systematic effects in quadrature as

$$\left\langle \frac{\sigma_{\text{systematics}}}{\sigma_{\text{statistical}}} \right\rangle = \sqrt{\sum_i^{\text{all systematics}} \left\langle \frac{\sigma_{\text{systematics},i}^2}{\sigma_{\text{statistical}}^2} \right\rangle}, \quad (2.23)$$

where all the systematic effects considered are summarized in Tab. 2.7.

Systematic error	$\langle \sigma_{\text{systematic}}/\sigma_{\text{statistical}} \rangle$	$\langle \sigma_{\text{systematic}} \rangle$	$\langle \sigma_{\text{statistical}} \rangle$
Period compatibility	0.0	0.0	0.039
Acceptance fluctuation	0.2	0.008	0.039
False asymmetry	0.5	0.020	0.039
Left-Right migration	0.09	0.004	0.039
Total	0.55	0.021	0.039

Table 2.7: Summary of systematic error impacts to the integrated asymmetry

2.4 Results

The asymmetries in this analysis are calculated from each of the separate nine periods and then combined as a weighted average. This calculation method is used to minimize the effects of acceptance changes between periods as the spectrometer was kept stable within each period but had the options for detector changes and repairs between periods. This resulting asymmetry for each method is determined from a weighted average as

$$A_N = \sum_{\text{period}} \frac{A_{N,\text{period}} \sigma_{\text{period}}^{-2}}{\sigma_{\text{period}}^{-2}}, \quad \sigma^2 = \sum_{\text{period}} \frac{1}{\sigma_{\text{period}}^{-2}}. \quad (2.24)$$

The results for the basic geometric mean are shown in Fig. 2.17 and the results for the two target geometric mean are shown in Fig. 2.18. The systematic error bars are discussed in Sec. 2.3.

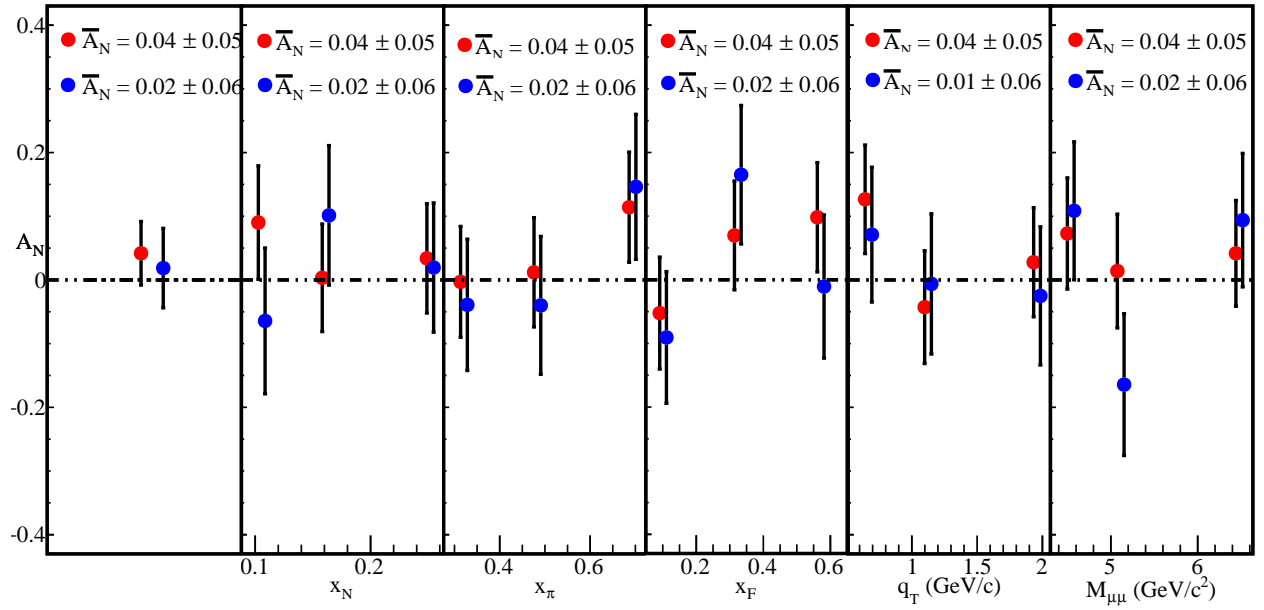


Figure 2.17: A_N determined from the geometric mean method for the upstream target (red) and the downstream target (blue)

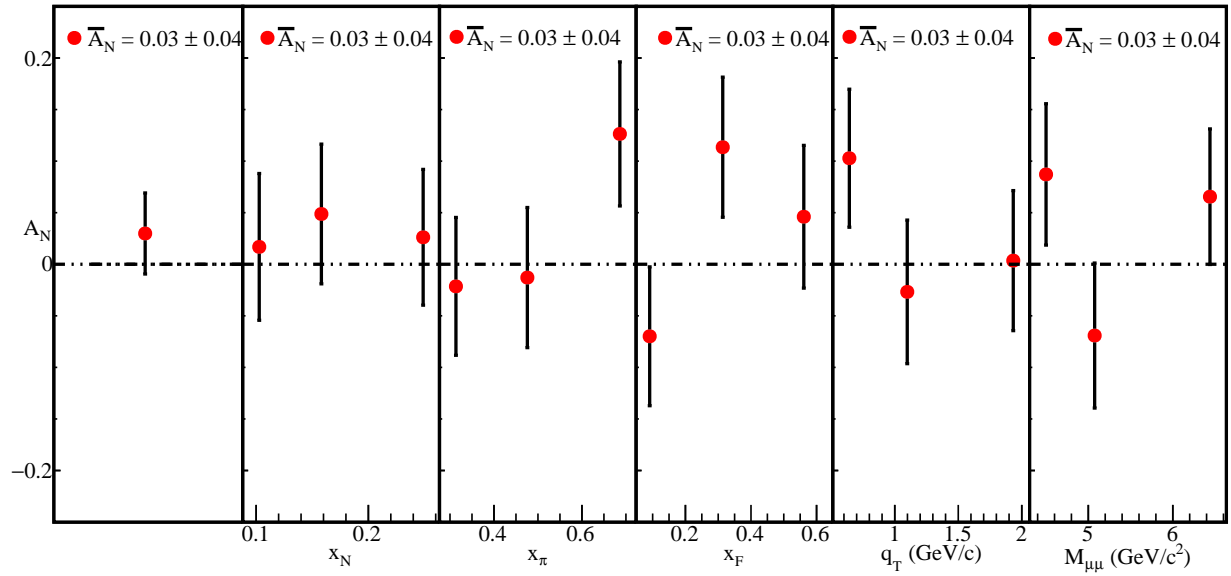


Figure 2.18: A_N determined by the geometric mean method using both targets simultaneously

2.4.1 Comparison of results

Appendix A

Systematic Error Derivations

A.1 Systematic Error From Acceptance

For an asymmetry defined as

$$A_\alpha = \frac{1}{P} \frac{\alpha\sigma_L - \sigma_R}{\alpha\sigma_L + \sigma_R} \quad (\text{A.1})$$

where α is an acceptance ratio. α is assumed to be close to unity therefore let

$$\alpha = 1 \pm 2 * \epsilon, \quad (\text{A.2})$$

where ϵ is a small positive number. The asymmetry can therefore be written

$$\frac{1}{P} \frac{(1 \pm 2 * \epsilon)\sigma_L - \sigma_R}{(1 \pm 2 * \epsilon)\sigma_L + \sigma_R} = \frac{1}{P} \frac{\sigma_L - \sigma_R \pm 2 * \epsilon * \sigma_L}{(\sigma_L + \sigma_R)(1 \pm \frac{2 * \epsilon * \sigma_L}{\sigma_L + \sigma_R})}. \quad (\text{A.3})$$

From there Taylor expand the denominator to get

$$A_\alpha \approx \frac{1}{P} \frac{\sigma_L - \sigma_R \pm 2 * \epsilon * \sigma_L}{(\sigma_L + \sigma_R)} * \left(1 \mp \frac{2 * \epsilon * \sigma_L}{\sigma_L + \sigma_R}\right) \quad (\text{A.4})$$

$$= A_N \pm \frac{1}{P} \frac{2 * \epsilon * \sigma_L}{\sigma_L + \sigma_R} \mp A_N * \frac{2 * \epsilon * \sigma_L}{\sigma_L + \sigma_R} \mp \frac{1}{P} \left(\frac{2 * \epsilon * \sigma_L}{\sigma_L + \sigma_R} \right)^2.$$

Assuming A_N is small and $\sigma_L \approx \sigma_R$

$$A_\alpha \approx A_N \pm \frac{\epsilon}{P}. \quad (\text{A.5})$$

The true asymmetry can now be written

$$A_{N,\text{systematic}} \approx A_\alpha \mp \frac{\epsilon}{P}. \quad (\text{A.6})$$

Including the $\frac{\epsilon}{P}$ term as an additive error and using standard error propagation the systematic error can be approximated as

$$\delta A_{N,\text{systematic}} = \frac{|\alpha - 1|}{2} \frac{1}{P} + \frac{\delta_{\frac{|\alpha-1|}{2}}}{P}. \quad (\text{A.7})$$

A.2 Systematic Error From Left-Right Event Migration

Assuming the fraction of events miss-identified is γ and that the amount of miss-identified events reconstructed left equals the amount of outgoing events reconstructed right

$$A_{N,\text{measure}} = \frac{1}{P} \frac{(L + \frac{\gamma}{2}N_{\text{total}}) - (R + \frac{\gamma}{2}N_{\text{total}})}{(L + \frac{\gamma}{2}N_{\text{total}}) + (R + \frac{\gamma}{2}N_{\text{total}})} = \frac{1}{P} \frac{L - R}{(L + R) * (1 + \gamma * \frac{N_{\text{total}}}{L + R})}, \quad (\text{A.8})$$

where N_{total} is the total events measure, L is the true events measured to the left that should be measured left and R is the number of events measure to the right that should be measured to the right.

Assuming γ is a small percentage, the denominator can be Taylor expanded to give

$$A_{N,\text{measure}} \approx A_N \left(1 - \gamma * \frac{N_{\text{total}}}{L + R} \right). \quad (\text{A.9})$$

Including $\gamma A_{N,\text{measure}}$ as an additive error and using standard error propagation the systematic error can be approximated as

$$\delta A_{N,\text{systematic}} = \gamma * A_{N,\text{measure}} + \gamma * \delta A_{N,\text{measure}}. \quad (\text{A.10})$$

References

- [1] P. Abbon et al. The COMPASS experiment at CERN. *Nucl. Instrum. Meth.*, A577:455–518, 2007.
- [2] A. Abragam and M. Goldman. Principles of dynamic nuclear polarisation. *Reports on Progress in Physics*, 41:395–467, 1978.
- [3] V. Yu. Aleksakhin, Y. Bedfer, S. Gerasimov, and A. Yu. Korzenev. Geometrical event reconstruction in the COMPASS experiment. *Phys. Part. Nucl. Lett.*, 4:350–362, 2007. [Pisma Fiz. Elem. Chast. Atom. Yadra2007,no.4,588(2007)].
- [4] Radja Boughezal, John M. Campbell, R. Keith Ellis, Christfried Focke, Walter Giele, Xiaohui Liu, Frank Petriello, and Ciaran Williams. Color singlet production at NNLO in MCFM. *Eur. Phys. J.*, C77(1):7, 2017.
- [5] R. Fruhwirth. Application of Kalman filtering to track and vertex fitting. *Nucl. Instrum. Meth.*, A262:444–450, 1987.
- [6] Torbjrn Sjstrand, Stefan Ask, Jesper R. Christiansen, Richard Corke, Nishita Desai, Philip Ilten, Stephen Mrenna, Stefan Prestel, Christine O. Rasmussen, and Peter Z. Skands. An Introduction to PYTHIA 8.2. *Comput. Phys. Commun.*, 191:159–177, 2015.